ACS NANO

www.acsnano.org

Article

Abnormal Chiral Coupling for Efficient and Stable Reduced-Dimensional Perovskite Emitters

Zicheng Li, Xinyu Duan, Hanting Meng, Tao Man, Nan Gong, Lin-Han Li, Zehui Zhou, Can Wang, Gongxun Bai, Zhi Chen, Zhenhuang Su, Xingyu Gao, Xiaofeng Liu, Weidong Shen, Wei Qin, Peng Gao, YuHuang Wang, Lijun Zhang, Ping-Heng Tan, Hailong Chen, Jianrong Qiu, Yuanhui Sun,* and Beibei Xu*

Cite This: *ACS Nano* 2026, 20, 9192−9204

Read Online

ACCESS | Metrics & More | Article Recommendations | Supporting Information

ABSTRACT: Highly efficient and stable reduced-dimensional halide perovskite (RDP) emitters are of vital importance for perovskite optoexcitonic devices. However, simultaneous improvement of their luminescence efficiency, stability, and phase purity based on principles without using external passivators has been a tremendous challenge. Here, an abnormal chiral coupling effect is introduced in the chiral benzene halide RDPs. Our strategy facilitates the construction of the network of both short-range nanoscale lattices and long-range superstructures, which leads to improved phase purity, reduced defects, weakened exciton−phonon scattering, and efficient excited-state transfer pathways. Consequently, an increment of photoluminescence quantum yield by over 35% compared to that of achiral counterpart was realized. This strong chiral coupling effect also enables the realization of stable and low threshold continuous wave lasing over 0.5 h at room temperature. Our study introduces an improved design principle for RDPs to control the defects, phase purity, crystal nano/microstructure, molecular interaction, and excited-state process for highly efficient and stable perovskite optoexcitonic devices.

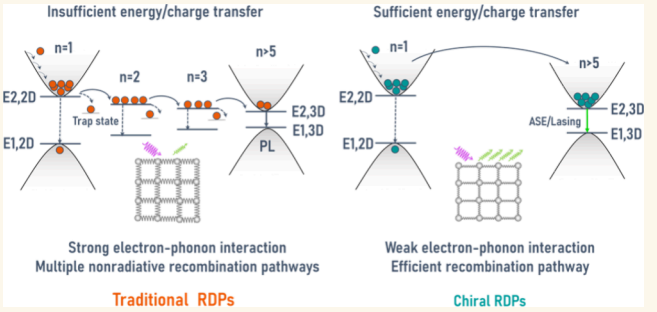

KEYWORDS: *chiral perovskites, structural order, exciton−LO phonon coupling, excited-state transfer, low-threshold CW lasing*

INTRODUCTION

RDPs have been regarded as a promising family of metal halide materials with superior properties. Compared to their 3D counterparts, the improvement of their efficiency and stability remains challenging for mixed-phase RDPs, which however is of vital importance for high performance light-emitting diodes,[1] lasers,[2] solar cells,[3] and photodetectors.[4] Despite significant advancements, several critical issues remain hindering the realization of this goal: (i) Besides the use of external passivators,[5] there is a lack of other internal methods for decreasing the density of defects and increasing the stability.[6−10] (ii) The mechanisms leading to the inefficient cascade excited-state transfer (EST) across multiple quantum wells (QWs) have yet to be unraveled.[11,12] The inefficient EST is generally associated with the quenching by defects and nonradiative energy loss across multiple steps of transfer, the random distribution, uncontrollable ratio of the crystalline domain, and the anisotropic transport of photoexcited charge carriers and energy.[13,14] Hence, the reduction of the density of defects, the optimization of the EST pathway, and the precise control of phase purity are necessary.

To realize the above goal, the design of RDP materials with customized structures and functions is of pivotal importance. However, traditional RDPs tend to form multiple QWs, and most studies are limited to the nanoscale lattice network, while the overall long-range superstructure network has been long overlooked. A primary reason is that most organic components in traditional RDPs do not affect the overall long-range network of the resultant compounds. Recently, chiral perovskites built up from chiral organic structures are drawing intensive attention, endowing RDPs with multiple functions. This initiates the exploration of circularly polarized photodetection,[15] spin manipulation emission polarization,[16] nonlinear chiroptical effects,[17] ferroelectricity,[18] spin Seebeck,[19] and chirality-induced spin selectivity.[20] Beyond these functionalities in chiral perovskites, previous studies on other chiral

Received: October 23, 2025
Revised: March 3, 2026
Accepted: March 3, 2026
Published: March 13, 2026

https://doi.org/10.1021/acsnano.5c18306
ACS Nano 2026, 20, 9192−9204

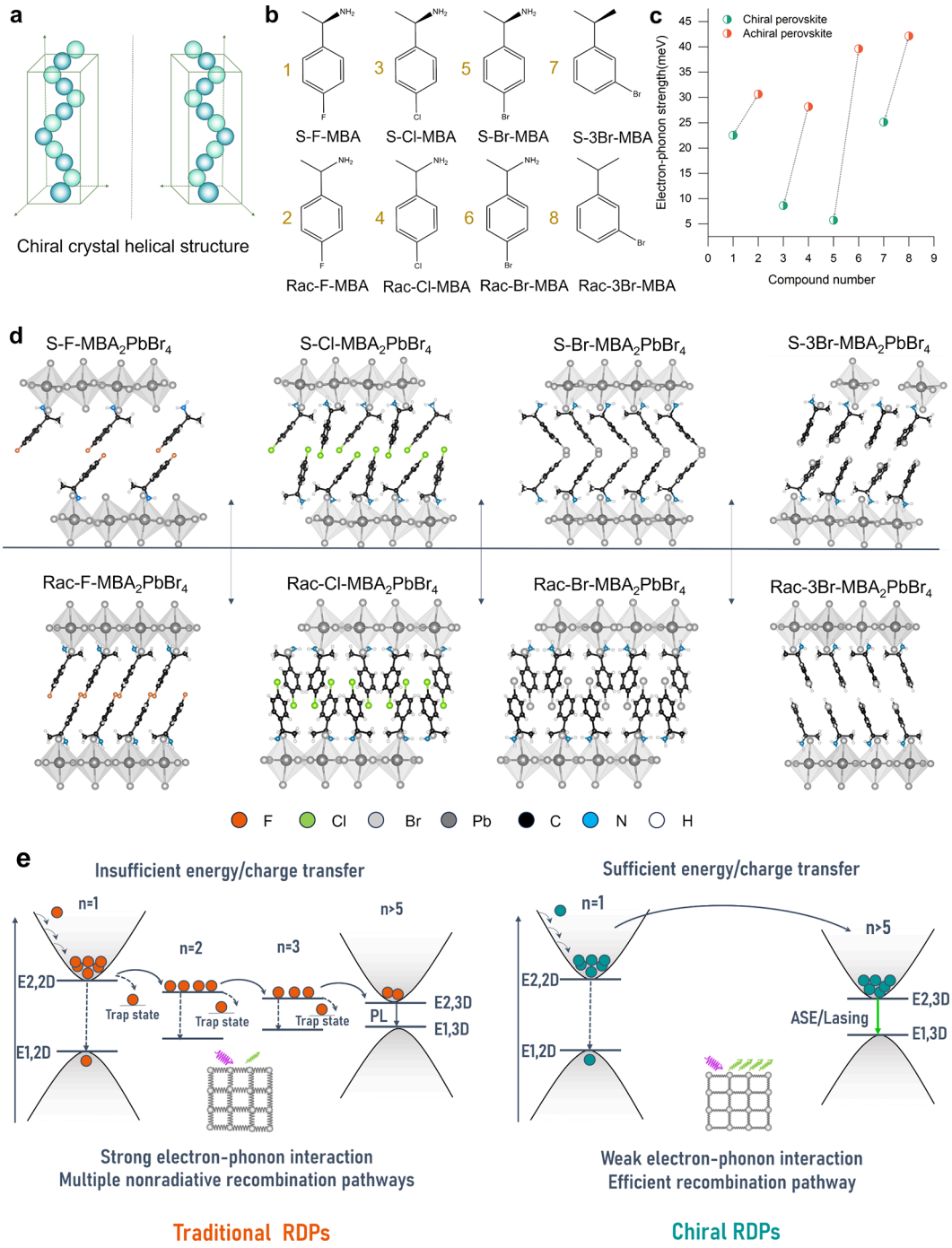

Figure 1. (a) Schematic diagram of the helical symmetric superstructure in the chiral crystal. (b) Organics used as cations for chiral and achiral perovskites. Each organic has been assigned a compound number and abbreviation. (c) Statistical plot of exciton−LO phonon coupling strength derived from temperature-dependent absorption spectra for chiral and corresponding achiral 2D perovskites. (d) Chiral and corresponding achiral two-dimensional perovskite crystal structures resolved by single-crystal XRD. (e) The chiral RDPs exhibit less defects and weaker exciton−LO phonon interaction induced via chiral-ordering, promoting sufficient excited-state transfer (EST) and leading to population inversion that generates amplified spontaneous emission (ASE)/lasing. The traditional RDPs exhibit strong exciton−LO phonon coupling and multiple nonradiative recombination channels originating from phase heterogeneity, resulting in inefficient energy transfer and population inversion.

compounds demonstrate that chirality can significantly affect the structures of materials. This includes breaking symmetry in chiral ferroelectrics to raise the Curie temperature,[21,22] coupling of photons and spin to induce magnetism by chiral light at room temperature,[23] and control of excitonic structure to achieve chiral superconductivity[24] and topological orbital texture.[25] Therefore, it would be of high interest to explore whether RDPs with a specific chiral structure could exhibit both the short-range nanoscale lattice network and the long-range superstructure network, such that defects, phase purity, EST pathways, and stability can be controlled to optimize the optoexcitonic properties.

Here, a series of chiral organic cations were incorporated into perovskite structures to induce chiral stereoisomeric configurations and helical architectures (Figure 1a). RDPs based on a wide variety of chiral and achiral organic

https://doi.org/10.1021/acsnano.5c18306
ACS Nano 2026, 20, 9192−9204

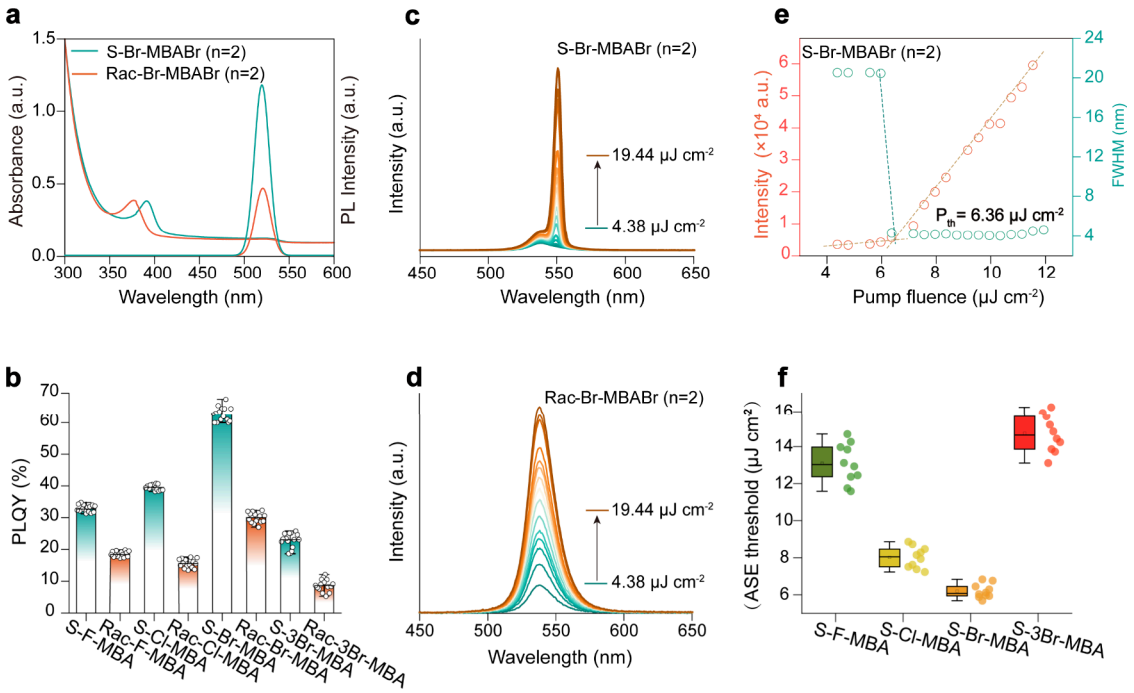

Figure 2. (a) The optical absorption and PL spectra of S/Rac-Br-MBABr (n = 2); (b) PLQY value of S/Rac-X-MBABr (n = 2, X = F, Cl, Br, 3Br); pump-fluence dependent emission spectra of (c) S-Br-MBABr (n = 2) and (d) Rac-Br-MBABr (n = 2); (e) pump fluence dependent PL intensities and the full width at half-maximum (fwhm) change of S-Br-MBABr (n = 2). (f) ASE threshold statistics plot of S-X-MBABr (n = 2, X = F, Cl, Br, 3Br).

candidates—with aromatic backbones—are synthesized and examined (Figure 1b). It is found that the two-dimensional perovskites incorporating tailored chiral benzene halide molecules S-X-MBA (X = F, Cl, Br, 3Br) promoted the formation of pure-phase RDP films with an exclusively n = 1 phase to decrease EST pathways. The chiral coupling effect plays a role through three synergetic mechanisms: (1) control the distortion of inorganic octahedra (Figure S1); (2) organization of ordered zigzag-type mechano-interlocked networks via interlayer/intralayer molecular forces (Figure 1d); and (3) formation of a helical symmetric superstructure (Figure 1a).[26] The latter two play a more critical role in enhancing both short- and long-range organic and inorganic lattice rigidity in contrast to the traditional concept of ordered inorganic layers alone. This chiral coupling effect decreases trap density, weakens exciton−LO phonon coupling (Figure 1c), reduces EST pathways, and facilitates enhanced EST efficiency in RDPs (Figure 1e). It ultimately enables room-temperature continuous-wave perovskite lasers with low threshold and long-time stability reported for the first time and over 35% increment of photoluminescence quantum yield (PLQY) compared to that of its achiral counterpart. Our work introduces a perspective on the understanding and control of the efficiency and stability of RDP emitters by the design of specific chiral structure. This will promote the development of RDP materials and highly efficient and stable RDP optoexcitonic devices.

RESULTS AND DISCUSSION

Optical Properties of Perovskite Films

Mixed phase (S/Rac-XMBA)$_2$FAPb$_2$Br$_7$ and pure phase (S/Rac-X-MBA)$_2$PbBr$_4$ (X = F, Cl, Br, and 3Br) chiral/achiral quasi-2D and pure 2D perovskite films are named as S/Rac-X-MBABr (n = 2) and S/Rac-X-MBABr (n = 1), respectively. All of the steady-state absorption spectra of both chiral and achiral quasi-2D perovskite films (Figure 2a and Figure S2) exhibit two peaks in the ultraviolet (UV) and green regions, corresponding to exciton absorption in the n = 1 phase and the 3D FAPbBr$_3$ phase, respectively. PL spectra exhibit emission from the 3D FAPbBr$_3$ phase (Figure 2a). Compared with that of the achiral counterpart, the exciton absorption peak of S-X-MBABr (n = 1) (X = Cl, Br) has a red-shift (Figure S3), indicating that chiral organic cations cause less inorganic octahedron distortion than their achiral counterparts.[27−29] All chiral quasi-2D perovskite films exhibit higher PLQY compared to their achiral counterparts, with the bromine-substituted variant showing the highest value. The PLQY of the S-Br-MBABr (n = 2) is 65%, significantly higher than the 30% of the achiral perovskite film (Figure 2b), indicating reduced losses from nonradiative recombination in the chiral counterpart.[30,31]

The chiral structure significantly influences the gain properties (Figure 2c,d and Figure S4). No amplified spontaneous emission (ASE) is observed in the achiral counterpart at the pumping density used in our work (Figure 2d, Figure S4b,e,h), while the chiral counterpart shows a lower threshold, with the lowest ASE threshold of 6.36 μJ cm^{-2} for S-Br-MBABr (n = 2) (Figure 2e,f and Figure S4c,f,i). Moreover, the obtained ASE threshold of S-Br-MBABr (n = 2) is lower than those of previous studies under the same n value (Table S1), confirming the advantage of the chiral coupling effect in RDPs for lasing application.

Structure and Excited State Dynamics of Perovskite Films

In the following discussion, we will primarily focus on the system represented by S-Br-MBA, with other relevant data provided in the Supporting Information. X-ray diffraction (XRD) confirms the phase purity of the crystals with n = 1 and

https://doi.org/10.1021/acsnano.5c18306
ACS Nano 2026, 20, 9192−9204

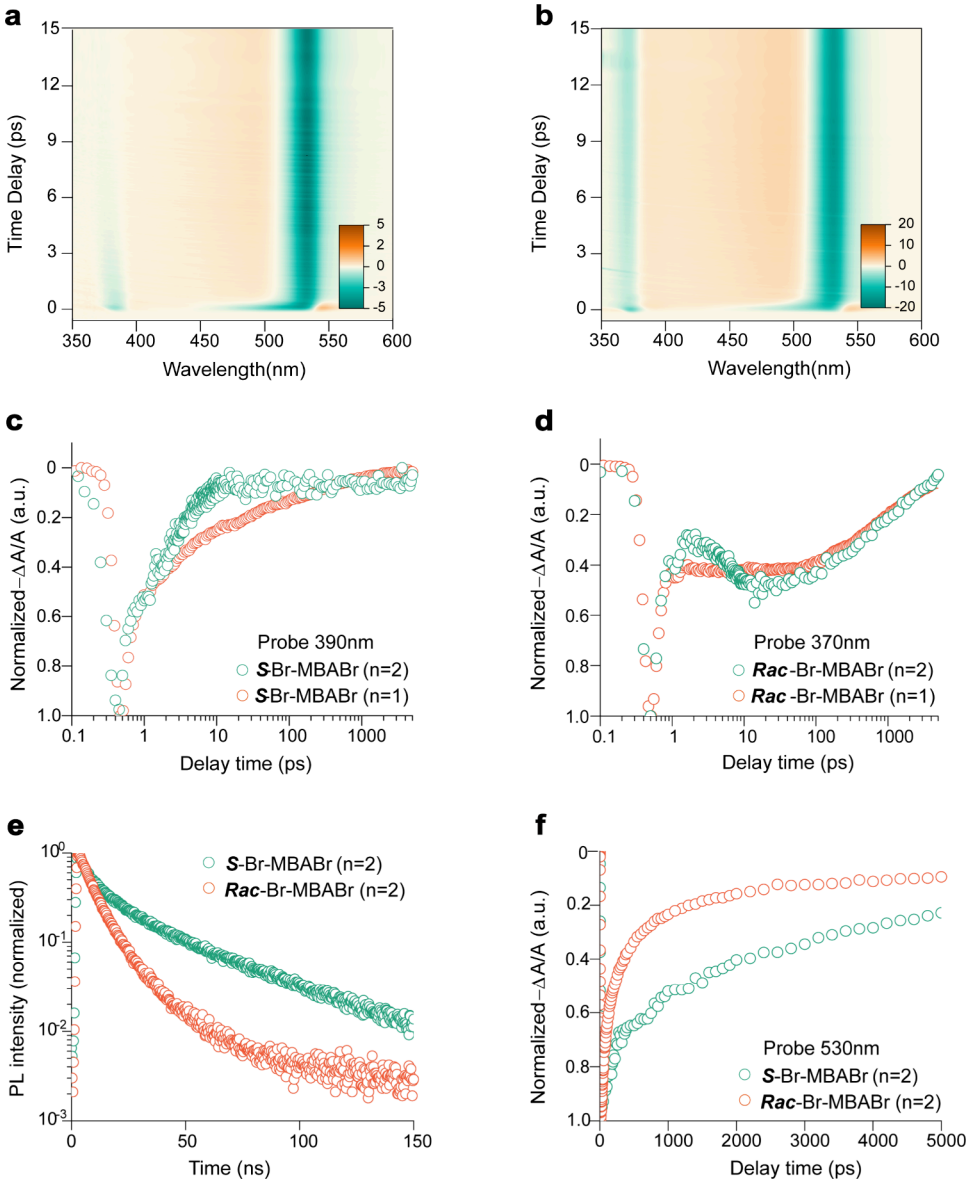

Figure 3. Excited-state dynamics of chiral and achiral perovskite films. False-color 2D TA maps of (a) chiral S-Br-MBABr (n = 2) and (b) achiral Rac-Br-MBABr (n = 2) films. TA carrier kinetics probed at the exciton absorption peak for (c) S-Br-MBABr (n = 1, 2) and (d) Rac-Br-MBABr (n = 1, 2) films. (e) Time-resolved PL and (f) TA carrier kinetics probed at 530 nm of S/Rac-Br-MBABr (n = 2).

3D phases (Figure S5). This is consistent with the absorption spectra indicated in the analysis above. There is no noticeable difference in domain distribution, surface morphology, and roughness for both chiral and achiral samples (Figures S6 and S7), excluding their significant effects on optical performance.

The transient absorption (TA) spectra of the chiral and achiral RDP films are compared (Figure 3a,b). The films exhibit two pronounced ground-state bleach (GSB) peaks centered at 394 (372 nm) and 535 nm (531 nm), originating from the excited state filling of 2D (n = 1) and 3D phases, respectively. The peak positions of these transitions are consistent with those observed in the steady-state absorption spectra (Figure 2a). The chiral RDP film exhibits a faster transfer dynamics process from the 2D to 3D phase (Figure 3a,b and Figure S8). The chiral RDP film exhibits a more rapid and obvious decay of the 390 nm excitonic signal compared with the chiral pure 2D perovskite film (Figure 3c). This indicates an increasingly efficient EST from the n = 1 chiral phase to adjacent 3D phases (Figure 3c and Figure S8a). However, the signal of achiral 2D and RDP films exhibits an initial decline followed by a slight increase; concurrently, the exciton resonance at the GSB of the n = 1 phase lasts for a long excitation time (1000 ps; Figure 3d and Figure S8b). The results indicate that excitons persistently accumulated in the n = 1 phase in the first dozen ps for the achiral sample, leading to incomplete EST between the different phases and weak population inversion for ASE.[32] Assuming that all the ESTs mentioned here are attributed to energy transfer, the TA spectra reveal that the chiral perovskite (64%) exhibits a nearly 60% higher energy transfer efficiency compared to its achiral counterpart (5%).[33] Pump fluence-dependent TA spectra (Figure. S9) reveals that the disparity in EST kinetics could partly be attributed to a higher prevalence of defect sites in the nonchiral 2D phase. These defects trap charge carriers, thereby resulting in diminished transfer efficiency.[34,35] These results are consistent with higher PLQY for the chiral counterpart.

https://doi.org/10.1021/acsnano.5c18306
ACS Nano 2026, 20, 9192−9204

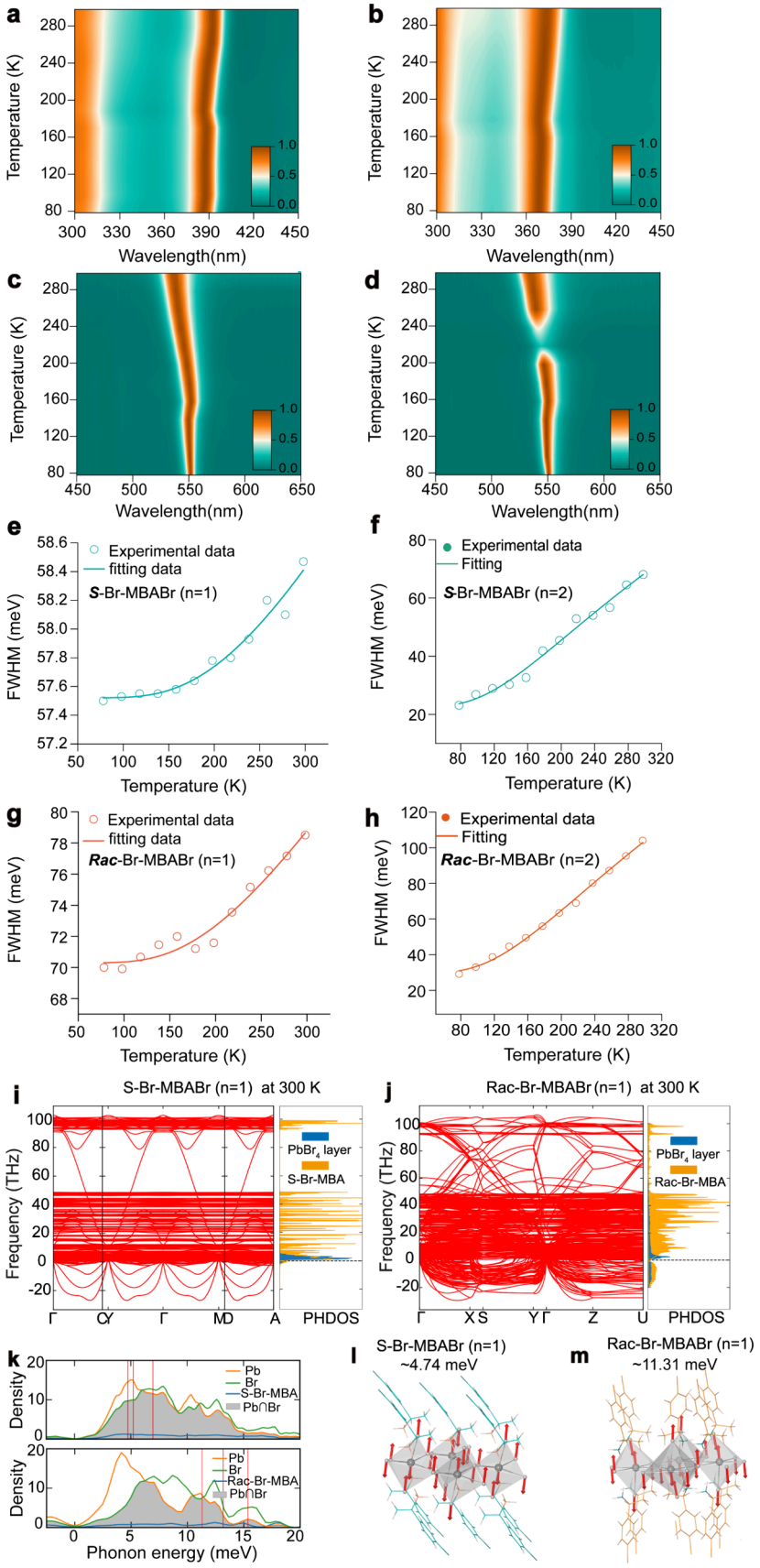

Figure 4. Quantification of exciton−phonon interactions. Contour maps of the temperature-dependent normalized steady-state absorption spectra of (a) S-Br-MBABr (n = 1) and (b) Rac-Br-MBABr (n = 1), from 298 to 78 K with 20 K intervals. Contour maps of the temperature-dependent steady-state normalized PL spectra of (c) S-Br-MBABr (n = 2) and (d) Rac-Br-MBABr (n = 2) films obtained under continuous wave (CW) laser excitation at 405 nm, and from 298 to 78 K with 20 K intervals. Temperature-dependent fwhm for the absorption spectra of (e) S-Br-MBABr (n =

https://doi.org/10.1021/acsnano.5c18306
ACS Nano 2026, 20, 9192−9204

Figure 4. continued

1) and (f) Rac-Br-MBABr (n = 1), and PL spectra of (g) S-Br-MBABr (n = 2) and (h) Rac-Br-MBABr (n = 2). The green or yellow dot represents the experimental data, and the corresponding solid lines represent the fitting results of the exciton−phonon coupling model. Phonon band structure and phonon density of states (PHDOS) of S-Br-MBABr (n = 1) and Rac-Br-MBABr (n = 1) at 300 K (i,j), respectively. (k) The calculated phonon density of states of S/Rac-Br-MBABr (n = 1) within the low-frequency range (<20 meV), the red vertical lines correspond to the lowest frequency LO phonon modes. Contributions from Pb, Br, S/Rac-Br-MBA, and intersection of Pb and Br (Pb ∩ Br) are colored yellow, green, blue, and gray, respectively. (l,m) The lowest frequency LO phonon modes in S/Rac-Br-MBABr (n = 1), where red arrows indicate the direction of atomic vibrations.

TRPL spectroscopy reveals an average recombination lifetime (τ_{avg}) of 12.7 ns for the 3D phase in the chiral RDP film (Figure 3e), representing a 1.7-fold increase compared to that of the achiral film (7.6 ns). This is consistent with the TA dynamic (3D phase) spectroscopy analysis (Figure 3f), supporting the previous discussion of efficient EST in the chiral RDP film.

Exciton−Phonon Interaction Dynamics

To elucidate the mechanistic origins of the disparate excited-state relaxation kinetics, the exciton−phonon interaction strength was monitored using temperature-dependent fwhm analysis of the stable-state absorption (Figure 4a,b, Figures S10−S12) and PL spectra (Figure 4c,d, Figure S13).[36] The temperature-dependent characteristics in most semiconductors can be explained using first-order perturbation theory with a focus on four scattering mechanisms (Supporting Information, Note 1). The correlation between the fwhm of chiral and achiral 2D perovskites and temperature was fitted via the LO phonon dominating model. It can be simplified as eq 1.[37]

$$\Gamma(T) = \Gamma_0 + \frac{\Gamma_{LO}}{\exp\left(\frac{E_{LO}}{k_B T}\right) - 1} \quad (1)$$

where Γ_0 is a temperature-independent constant that arises from scattering due to structural disorder/imperfection scattering,[38] Γ_{LO} is the exciton−longitudinal optical (LO) phonon coupling strength, E_{LO} is the longitudinal optical phonon energy, T is the temperature, and k_B is the Boltzmann constant. The fwhm of the absorption and PL spectra is extracted, and then, the curve is fitted according to eq 1 as shown in Figure 4e−h. S-Br-MBABr (n = 1) has a lower coupling strength than Rac-Br-MBABr (n = 1) (5.72 meV versus 39.6 meV). This indicates weaker exciton−LO phonon coupling strength and suppressed structurally vibrational relaxation in S-Br-MBABr (n = 1). Furthermore, the exciton−LO phonon coupling in the 3D phase for S-Br-MBABr (n = 2) is significantly lower than that of Rac-Br-MBABr (n = 2) (52.1 vs 124.2 meV), indicating the strong interaction between the 3D domain and the 2D chiral domain (Figure 4g,h). The reduced Fröhlich coupling constant in 2D and 3D phases further supports S-Br-MBABr (n = 2) to achieve enhanced EST efficiency and fast population inversion through lattice vibration suppression. All of the other chiral 2D perovskites also demonstrate significantly reduced exciton−LO phonon coupling relative to that of achiral analogues (Figure S14 and Table S2). Among them, the S-Br-MBABr (n = 1) system exhibits the weakest exciton−LO phonon coupling, which aligns well with the observed trends in ASE thresholds and PLQY.

To enhance the understanding of how chiral differences are formed, further insights are obtained by investigating the phonon characteristics of Rac/S-Br-MBABr (n = 1) using DFT calculations. Considering the non-negligible effect of temperature on anharmonic vibration in perovskites, we use ab initio molecular dynamics (AIMD) simulations and mode decomposition techniques to measure the anharmonic phonon line width and frequency shift of Rac/S-Br-MBABr (n = 1) at 0 K (Figure S15) and 300 K (Figure 4i,j).[39] The results indicate that the imaginary frequency intensity contributed by the inorganic layers in S−Br-MBABr (n = 1) progressively decreases, whereas the imaginary frequency broadening of the inorganic layers in Rac-Br-MBABr (n = 1) increases markedly (Figure 4i,j). The increased concentration of imaginary frequency in Rac-Br-MBABr (n = 1) indicates a greater degree of lattice instability, which enhances phonon scattering. Since phonons serve as the primary carriers of heat conduction, the scattering process impedes their ability to propagate within the lattice. In lead halide perovskite, excited LO phonons from the inorganic component are essential in phonon−exciton interaction and phonon−phonon scattering processes.[40−42]

Figure 4k illustrates the calculated phonon density of states for S/Rac-Br-MBABr (n = 1) in the low-frequency range (<20 meV), with the red vertical lines representing the lowest frequency LO phonon modes. The highly ordered S-Br-MBABr (n = 1) has significantly lower LO phonon frequencies than Rac-Br-MBABr (n = 1). The LO phonon frequencies of highly ordered S-Br-MBABr (n = 1) range from 4 to 7 meV, while those of Rac-Br-MBABr (n = 1) are as high as 11−15 meV. Figure 4l,m depicts the lowest frequency LO phonon modes of S-Br-MBABr (n = 1) (∼4.74 meV) and Rac-Br-MBABr (n = 1) (∼11.31 meV), with red arrows indicating the direction of atomic vibrations. The remaining lowest-frequency LO phonon modes are depicted in Figure S16. Low-frequency LO phonons facilitate rapid phonon−exciton energy exchange, promoting efficient energy transfer. Furthermore, the density of the lowest frequency LO phonon modes in S-Br-MBABr (n = 1) is significantly higher than that in Rac-Br-MBABr (n = 1), providing more energy channels and thereby promoting the radiative recombination of the charge carrier.

Ordering of Lattice Structure

A tentative explanation for the reduced exciton−LO phonon coupling strength and reduced defects in chiral perovskite can be proposed based on the inspection of the structural ordering, including the inorganic perovskite cage and the intermolecular interactions. Rac-Br-MBABr (n = 1) crystallizes in the centrosymmetric space group *Pnma*, while chiral S-Br-MBABr (n = 1) adopts the helical symmetric space group $P2_12_12$ (Tables S3−S4). Single crystals of other systems are also systematically compared (Figures S17−S24 and Tables S5−S10). The distortion of the inorganic lattice plays an important role in lattice dynamics, which influences optical properties.[43] Table 1 and Tables S11 and S15 summarize the key metrics for quantifying structural distortions in the inorganic perovskite layer. To quantify the average distortion

https://doi.org/10.1021/acsnano.5c18306
ACS Nano 2026, 20, 9192−9204

Table 1. Comparison of the Structural Parameters for Chiral and Achiral 2D Perovskites

structure parameters	S-Br-MBABr (n = 1)	Rac-Br-MBABr (n = 1)
average Pb−Br bond length (Å)	3.0346	3.0893
standard deviation of bond length	0.0864	0.1826
difference between maximum and minimum bond lengths (Å)	0.2552	0.4222
average quadratic elongation λ	1.0003	1.0029
average equatorial Pb−Br−Pb angles (β)	152°	153°
difference between maximum and minimum bond angles (deg/in plane) $\Delta\beta$	11.4	10.8
distortion index (bond length) (D)	0.0204	0.0485
effective coordination number	5.842	5.280
bond angle variance (σ^2)	39	36
optical bandgap (eV)	3.74	3.91

degree of the intraoctahedron, the distortion index (D, bond length), bond angle variance (σ^2), and bond length quadratic elongation ($\langle\lambda\rangle$) are calculated by using eqs 2−4:[30,44]

$$D = \frac{1}{6}\sum_{\{i=1\}}^{6}\frac{|d_i - d_0|}{d_0} \tag{2}$$

$$\sigma^2 = \left(\frac{1}{11}\right)\sum_{\{i=1\}}^{12}(\theta_i - 90)^2 \tag{3}$$

$$\langle\lambda\rangle = \frac{1}{6}\sum_{\{i=1\}}^{6}\left(\frac{d_i}{d_o}\right)^2 \tag{4}$$

d_i denotes the six Pb−X bond lengths, and d_0 is the mean M−X bond length. θ_i corresponds to the octahedral Br−Pb−Br bond angles. For an ideal octahedron, both D and σ^2 are exactly 0. Chiral S-Br-MBABr (n = 1) exhibits a 2-fold decrease in the distortion index D (0.0204) and a higher inorganic lattice ordering (Figure 5a,b). Additionally, we employed ab initio molecular dynamics (AIMD) simulations to assess the impact of temperature (0 and 300 K) on structural changes (Figure S25 and Table S14). We further elucidate how chiral organic cations induce structural ordering by calculating the in-plane angular disparity (8.32° vs 10.68°) and out-of-plane halide displacement (5.2° vs 6.5°), where both are reduced, a trend consistent with that observed in the inorganic octahedra; detailed computational methods are provided elsewhere.[44] The results demonstrate that chiral organic cations not merely influence the structure through steric effects but also fundamentally reshape the distortion pattern of the octahedral network via symmetry breaking.

Combined with all single crystals, the result reveals that chiral perovskites in the S/Rac-X-MBA (X = Br, Cl) systems exhibit smaller octahedral distortion indices, while the S/Rac-X-MBA (X = F, 3Br) systems show reduced distortion in achiral configurations. However, as evidenced by temperature-dependent absorption spectra, all chiral 2D perovskites exhibit a weaker exciton−LO phonon coupling strength. This leads us to hypothesize that the distinct intermolecular interaction networks and the overall chiral helical symmetry play a more dominant role in enhancing the rigidity of the lattice structure than does the octahedral distortion. This abnormal phenomenon has never been observed before. All chiral 2D perovskites form ordered zigzag-type mechano-interlocked networks via interlayer or intralayer molecular forces through the synergistic effects of halogen bonding (XB) and hydrogen bonding (H···B), and rigid helical symmetric structure through chiral stereoisomeric configurations (Figure 5c,e and Figures S26, S28, S30), significantly enhancing lattice stability and rigidity. In contrast, such structural features are absent in their achiral counterparts (Figure 5d,f and Figures S27, S29, S31).

Furthermore, Figure 5g,i illustrates the characteristic phonon vibration modes associated with octahedral twisting in S-Br-MBABr (n = 1) and octahedral compression in Rac-Br-MBABr (n = 1) resulting from interactions with organic molecules. Additional related phonon vibration modes are depicted in Figure S32. The excitonic band structure analysis reveals that the Pb-6s orbitals at the valence band maximum (VBM) exhibit greater distortion in Rac-Br-MBABr (n = 1) with respect to S-Br-MBABr (n = 1) (Figure 5h−j). Moreover, the unoccupied Pb-6p orbitals at the conduction band minimum (CBM) become more localized in Rac-Br-MBABr (n = 1) (Figure 5h−j and Figure S33). These findings can be attributed to the increased octahedral distortion observed in Rac-Br-MBABr (n = 1), consistent with the structural analysis above.

Lasing Properties

We constructed a room temperature continuous wave (CW) green laser by sandwiching the perovskite film in a quartz matrix between a bottom distributed Bragg reflector (DBR) mirror and a top Ag mirror (320 nm), forming a Fabry−Pérot (F−P) cavity (Figure 6a, Figure S34). Figure S35 and Figure 6b,c show the emission spectra at varied pump intensities of a room temperature femtosecond laser and CW laser, revealing the emergence of lasing with the increased pump power. Figure 6d shows the corresponding light−light curve and the cavity mode line width−evolution curve.[45] The lasing threshold is 1.57 W cm^{-2}, which is one of the lower values ever reported at room temperature (Table S16). Simultaneously, the line width undergoes a rapid reduction. The superlinear intensity dependence is fitted to the power law $I = x^p$ with p = 7.2 above the threshold. The highest lasing quality factor is 1800 with a narrow fwhm of 0.3 at ∼555 nm, which is also the narrowest fwhm for a perovskite CW laser at room temperature (Figure 6e, Table S16). Meanwhile, the emission from the devices is typically linearly polarized. The degree of polarization (DOP = $(I_{max} - I_{min})/(I_{max} + I_{min})$, where I_{max} and I_{min} are the maximum and minimum emission intensities) of the lasing mode is 75% (Figure 6f), significantly higher than that of the SE peak (<5%). As shown in Figure 6g, strong interference fringes are identified around the overlapping area between the real space and its inverted images, and the distance surpasses 15 cm, which indicates the buildup of long-range spatial coherence. Figure 6h and Figure S36 show green lasing with well-defined spatial coherence (beams) when operated above and below the threshold, respectively. These spectra clearly illustrate the line width-narrowing effect, linear-to-super linear transition, the first-order spatial coherence, and the dominance of lasing emission over spontaneous emission beyond the lasing threshold. Figure 6i shows that during continuous pumping for 30 min, the laser output intensity remains above 90% of its initial value, after which a slow decay trend is observed. This indicates that the device indeed maintains efficient and stable operation.

https://doi.org/10.1021/acsnano.5c18306
ACS Nano 2026, 20, 9192−9204

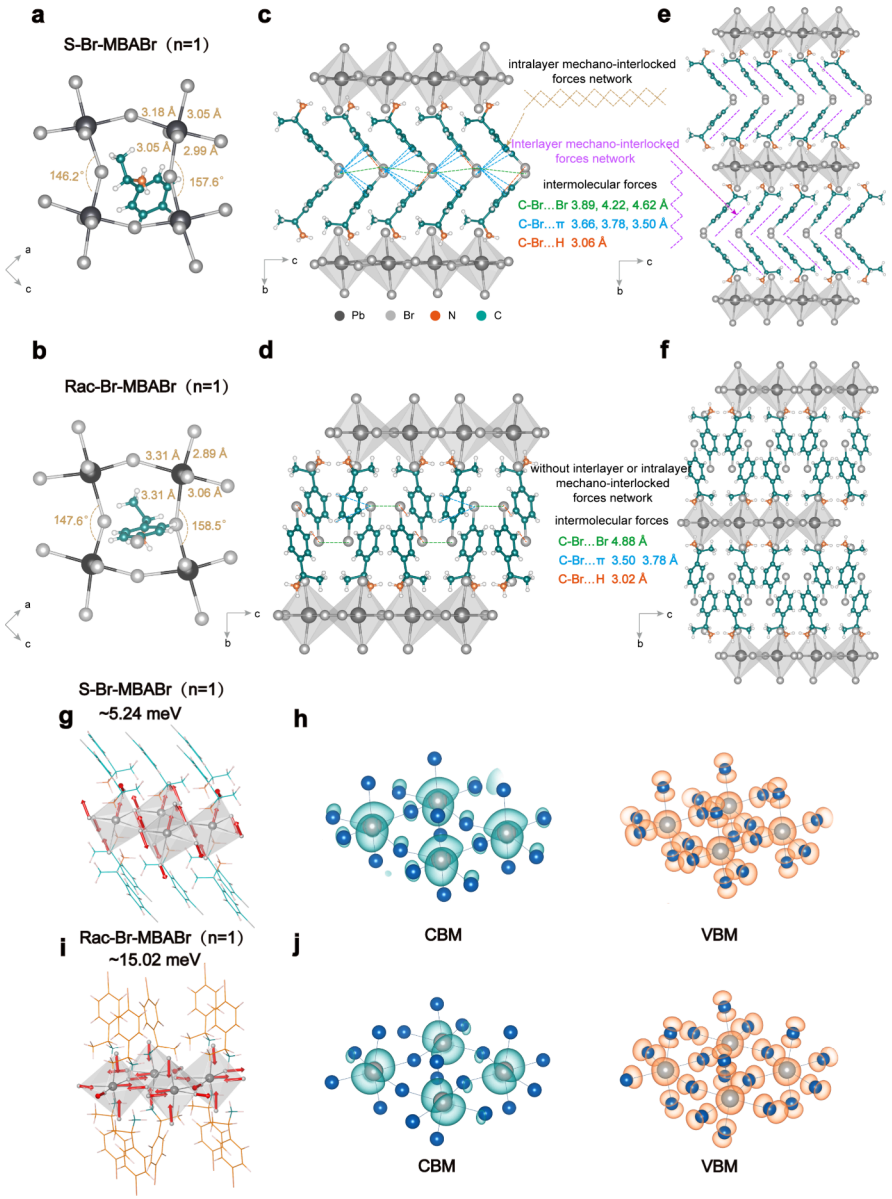

Figure 5. Top-down view of the crystal structures of (a) S-Br-MBABr (n = 1) and (b) Rac-Br-MBABr (n = 1). An in-plane distortion of the octahedra can be clearly observed. Single crystal structure and analysis of intermolecular interaction for (c,e) S-Br-MBABr (n = 1) and (d,f) Rac-Br-MBABr (n = 1). Participating phonon vibration modes are associated with (g) octahedral twisting in S-Br-MBABr (n = 1) and (i) octahedral compression in Rac-Br-MBABr (n = 1), where red arrows indicate the direction of atomic vibrations. Partial charge density for the CBM and VBM of (h) S-Br-MBABr (n = 1) and (j) Rac-Br-MBABr (n = 1).

CONCLUSIONS

Our study proposes a strategy to design low-entropy, halogen-containing chiral S-X-MBA (X = F, Cl, Br, 3Br) hybrid perovskite with an abnormal chiral coupling effect. This design introduces a chiral stereoselective effect, multiple inter/intramolecular interactions, ordered helical symmetric superstructure, and mechano-interlocked networks, excluding the inorganic octahedral distortion as the determined factor for emission efficiency. It increases lattice ordering and rigidity, weakens exciton−phonon scattering, and reduces the losses from defects, promoting phase purification and highly efficient excited-state transfer. Consequently, room-temperature low threshold, stable continuous-wave lasers, and over 35% increment of PLQY compared to that of its achiral counterpart were realized. A bright perspective was introduced, that is, the design of chiral perovskites with an enhanced network for both short-range nanoscale lattices and long-range superstructures. The methods for decreasing defects, increasing phase purity, and smoothing the dynamic excited-state transfer pathways will promote the development of highly efficient and stable perovskite optoexcitonic devices.

METHODS

Starting Materials

Formamidinium bromide (FABr, >99.99%), methylammonium bromide (MABr, >99.99%), and lead bromide ($PbBr_2$, >99.99%) were purchased from Advanced Election Technology Co., Ltd. (*S*)-(−)-4-Bromo-alpha-phenylethylamine (S)-BrMBA and (racemic)-(−)-4-bromo-alpha-phenylethylamine (Rac)-BrMBA were purchased from Alfa Aesar. (*S*)-4-Fluoro-alpha-methylbenzylamine (S)-FMB,; 4-fluoro-alpha-methylbenzylamine (Rac)-FMBABr, (*S*)-1-(4-

https://doi.org/10.1021/acsnano.5c18306
ACS Nano 2026, 20, 9192−9204

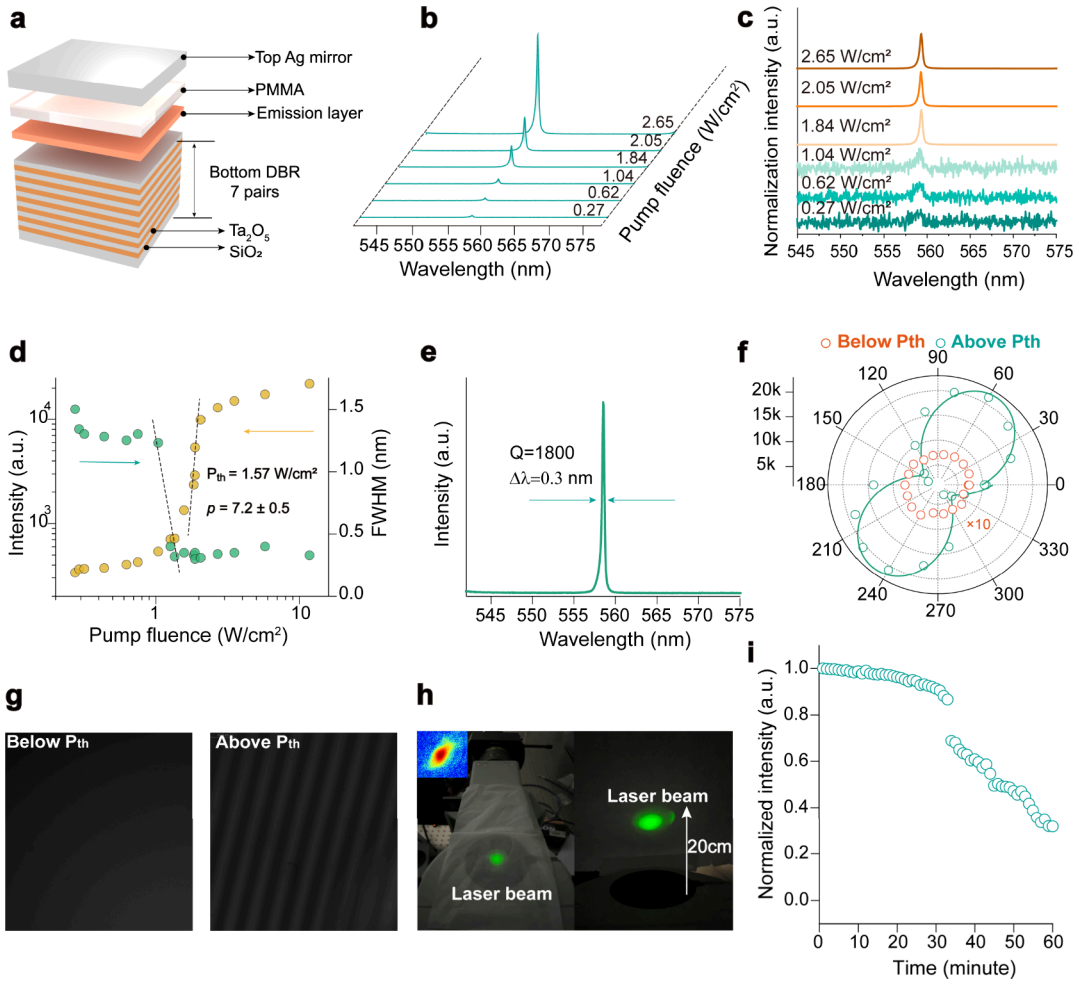

Figure 6. Lasing properties. (a) Schematic structure of the lasing device with an emission layer sandwiched between DBR and Ag mirror. (b) Evolution of PL spectra under various pump fluences by 405 nm CW laser excitation. (c) Evolution of normalized PL spectra under various pump fluences by 405 nm CW laser excitation. (d) Corresponding PL intensity against increasing pump fluences on the log−log scale. (e) PL spectrum of the laser above threshold. (f) Polar plots of emission intensity at pump fluences below (orange) and above (green) the threshold. (g) The image of the Michelson interferometer with two arms to probe the first-order spatial coherence below and above P_{th}. (h) PL images of a chiral S-Br-MBABr (n = 2)-based device with pump fluence above P_{th}. The top-left inset shows laser beam profiles captured by the beam profiler. (i) Lasing stability tests under 405 nm CW laser pumping at room temperature in air with a relative humidity of ~40−50%.

chlorophenyl)ethanamine (S)-ClMBA, 1-(4-chlorophenyl)-ethanamine (Rac)-ClMBA, (S)-1-(3-bromophenyl)ethylamine (S)-3BrMBA, and 1-(3-bromophenyl)ethylamine (Rac)-3BrMBABr were purchased from Aladdin. (S)-BrMBABr, (racemic)-BrMBABr, (S)-FMBABr, (racemic)-FMBABr, (S)-ClMBABr, (racemic)-ClMBABr, (S)-3BrMBABr, and (racemic)-3BrMBABr were purchased from Xi'an Polymer Light Technology Co., Ltd. Chlorobenzene (CB), DMF, and DMSO were purchased from Sigma-Aldrich. HBr (48 wt % in H_2O) was obtained from Alfa Aesar and used without further purification. Unless otherwise stated, all materials were used without purification.

Synthesis of Layered (S/Rac)-XMBA$_2$PbBr$_4$ (X = F, Cl, Br, 3Br) Single Crystals

Single crystals of all of the chiral MHPs studied here were grown by slowly cooling over 60 h from a hot (95 °C) aq. HBr solution of $PbBr_2$ and chiral amine in a 20 mL sealed vial in air. As a general synthesis procedure of layered perovskite single crystals, 0.5 mmol of $PbBr_2$ and 1 mmol of (S) or racemic-BrMBA were separately dissolved in 6 mL of HBr by heating at 95 °C for 30 min. On cooling the solution slowly from 95 °C to room temperature with a cooling rate of 1 °C/h, white single crystals formed gradually. The synthesis method of other single crystals is the same as above.

Preparation of Perovskite Solution

The perovskite precursor (S/Rac)-Br-MBA$_2$FAPb$_2$Br$_7$ was prepared by dissolving stoichiometric ratios of each of FABr, (S)-BrMBABr, (racemic)-BrMBABr, and $PbBr_2$ (chiral amine:FABr:$PbBr_2$ = 2:1:2 molar ratio) in DMSO at a concentration of 0.4 M. The solution was stirred for 12 h in a N_2-filled glovebox at room temperature and was filtered through 0.22 μm filters before use. The synthesis method of the other perovskite solution is the same as above.

Fabrication of Perovskite Films

Quartz glasses (15 mm × 15 mm, Advanced Election Technology Co., Ltd.) were sonicated in deionized water, acetone, and 2-propanol for 10 min each sequentially. The surface of the quartz glass substrates underwent oxygen plasma treatment for 10 min to achieve a hydrophilic surface. After treatment, the substrates were transferred to a N_2-filled glovebox for deposition of the perovskite layer. 50 μL of perovskite precursor solution was spin-coated onto precleaned quartz substrates at 1000 rpm for 10 s, then 5000 rpm for 50 s, during which 200 μL of CB solution was dropped onto the spinning perovskite film. The samples were annealed at 95 °C for 10 min. For transient absorption and luminescence measurements, 5 wt % PS CB solution was spin-coated onto the samples at 5000 rpm for 30 s for protection.

https://doi.org/10.1021/acsnano.5c18306
ACS Nano 2026, 20, 9192−9204

Fabrication of the Quasi-2D Perovskite Laser Device

The quartz glass was used as the substrate to construct the devices. A magnetron sputtering machine was employed to deposit oxide sources (SiO_2, Ta_2O_5, 99.9%). First, 7 pairs of 63.21 nm SiO_2 and 93.57 nm Ta_2O_5 were deposited alternately to fabricate the bottom DBR, followed by the prepared perovskite film via the spin-coating method. Then, PMMA (220 mg/mL) was spin-coated on the surface with a spin rate of 4000 rpm. Finally, 320 nm Ag was deposited as the top DBR. The bottom DBR mirror and top Ag mirror show high reflectivity (98.50% and 99.93%) at a wavelength of ∼550 nm.

Single-Crystal XRD and Powder XRD Measurement

Powder X-ray diffraction spectra were recorded using a SHIMADZU XRD-7000 X-ray diffractometer equipped with a 9 kV Cu Kα source. Single-crystal XRD structure analysis was performed at 298 K on a Bruker D8 VENTURE instrument (Mo Kα radiation, λ = 0.71073 Å operating at 50 kV and 30 mA). Structural parameters were obtained by SHELXT and refined by SHELXL. The crystallographic structure was then visualized by using VESTA and OLEX2 software.

AFM and SEM Measurement

Atomic force microscopy (AFM) (Bruker Dimension ICON) tests were conducted in tapping mode. SEM measurements were carried out on perovskite films deposited on quartz by a Zeiss Sigma300 SEM.

Ultraviolet−Visible Absorption and PLQY Measurement

Ultraviolet−visible (UV−vis) absorption spectra were collected by a UV−vis−NIR spectrometer (UH-5700, Hitachi, Japan). The absolute PLQY was obtained with a UV−NIR absolute photoluminescence quantum yield spectrometer (Quantaurus-QY Plus C13534-12, Hamamatsu Photonics, Japan).

Transient Absorption Spectra

Transient absorption spectroscopy was performed using the output of a Ti:sapphire fs laser amplifier system (Spitfire Ace, Spectra-Physics) of 800 nm centered wavelength, 70 fs pulse width, and 5 kHz repetition rate. Pump wavelength was tunable by pumping an optical parametric amplifier (TOPAS, Spectra-Physics), and the supercontinuum of the probe pulse was obtained by focusing the 800 nm pulses onto a 2 mm CaF_2.

Time-Resolved Photoluminescence Spectroscopy Measurement

PL decay curves were monitored at the PL center wavelength of each sample using an FL920 fluorescence spectrometer (Edinburgh Instruments, UK) under ambient conditions with 370 nm picosecond laser excitation. The data collected was based on time-correlated single photon counting (TCSPC).

Temperature-Dependent PL Spectral Measurement

For temperature-dependent PL measurements, polycrystalline thin films prepared on quartz substrates were mounted in a cryostat (INSTEC, HCP421 V-PM) with liquid nitrogen to control the measurement temperature. The samples were excited by continuous wave (CW) laser excitation at a wavelength of 405 nm and 20 K intervals.

Temperature Dependent Absorption Spectral Measurement

Temperature dependent absorption spectra was performed using an Avantes spectrometer (AvaSpec-ULS2048CL-EVO) with samples kept in a cryostat. Liquid nitrogen was used to control the temperature.

Lasing Characterizations

For ASE and femtosecond (fs) laser measurements, we used a home-built microscope setup for lasing PL spectroscopy measurement. The fundamental 1030 nm beam from a Yb:KGW laser (Pharos, Light Conversion Ltd.) with a temporal resolution of 212 fs was focused onto a barium metaborate (BBO) crystal to generate a high-power 343 nm excitation light (212 fs, 1 kHz) by third harmonic generation. The pump beam was focused onto perovskite film samples by a microscope with an objective. The emitted light from the samples was collected by the same objective lens and was collected by liquid nitrogen cooled detectors (NOVA highly sensitive spectrometer, ideaoptics, NOVA 2s and NOVA PG2000 with spectral resolutions of 0.18 and 0.07 nm, respectively) via a multimode fiber with the pump light filtered. For CW laser operation, a CW solid-state laser (405 nm, maximum power 50 mW; Sapphire SF, Coherent) was used to generate the excitation light. The excitation light was focused down to about 50 μm in diameter through a 5× objective (Renishaw, NA = 0.15), with input power altered by neutral density filters. The emitted light from the samples was collected by the same objective lens by semiconductor refrigeration detectors with a resolution of 0.05 nm (Renishaw inVia). The bottom DBR (7 pairs of SiO_2/Ta_2O_5) is designed to be highly transparent at the pump wavelength (reflectivity <5% at 405 nm). The top Ag mirror (320 nm) serves as a highly reflective back mirror (reflectivity ≈ 99.93% in the 400−750 nm range) and is opaque to the pump beam. The excitation laser (405 nm continuous-wave or 343 nm femtosecond pulsed) is thus designed to be incident from the DBR side and cannot penetrate the top Ag mirror. The generated fluorescence or lasing emission (∼550 nm) is reflected by the Ag mirror and exits from the DBR side. The excitation light (343 or 405 nm) is filtered out using an optical filter, so that only the coupled emission signal is detected by the spectrometer. The continuous-wave laser stability test was conducted in air without controlled environmental humidity, with the relative humidity maintained at approximately 50%.

First-Principles Density Functional Theory (DFT) Calculations

The underlying first-principles DFT calculations were carried out by using the plane-wave pseudopotential method as implemented in the Vienna Ab initio Simulation Package (VASP).[46] The exciton−ion interactions were described by the projector augmented wave pseudopotentials.[47,48] We used the generalized gradient approximation formulated by Perdew, Burke, and Ernzerhof as the exchange-correlation functional.[49] A kinetic energy cutoff of 520 eV was adopted for wave function expansion. Structures were fully optimized including van der Waals (vdW) interaction,[50] until the residual force was converged within 0.02 eV Å^{-1}. The k-point meshes were applied with an interval smaller than $2\pi \times 0.03$ Å^{-1} for the excitonic Brillouin zone to ensure that all enthalpy calculations converged within 0.02 eV/atom. Spin−orbit coupling was included in the excitonic structure calculations. The AIMD simulations lasted 20 ps with a time step of 2 fs based on an NVT ensemble with Nosé−Hoover temperature control within a 2 × 2 × 1 supercell for $(S\text{-Br-MBA})_2PbBr_4$ and a 2 × 1 × 2 supercell for $(Rac\text{-Br-MBA})_2PbBr_4$. Phonon dispersions were calculated by the real-space supercell method and the finite difference method implemented in the Phonopy code.[51] To consider the anharmonic effects, the DynaPhoPy code was employed to evaluate the phonon dispersions by extracting the phonon quasiparticles from AIMD simulations using the normal-mode-decomposition technique.[39]

■ ASSOCIATED CONTENT

Supporting Information

The Supporting Information is available free of charge at https://pubs.acs.org/doi/10.1021/acsnano.5c18306.

Optical properties of perovskite films: the optical absorption spectra of S/Rac-F-MBA (n = 2), S/Rac-Cl-MBA (n = 2), and S/Rac-3Br-MBA (n = 2) film; the optical absorption spectra of S/Rac-X-MBA (n = 1, X = F, Cl, Br, 3Br) films. The calculated band gap (E_g) and exciton binding energy (E_b); pump-fluence dependent emission spectra of S/Rac-F-MBA (n = 2), S/Rac-Cl-MBA (n = 2), and S/Rac-3Br-MBA (n = 2) films; crystallographic orientation characterization of chiral S-Br-MBABr (n = 2) and achiral Rac-Br-MBABr (n = 2)

https://doi.org/10.1021/acsnano.5c18306
ACS Nano 2026, 20, 9192−9204

films: 1D XRD patterns; SEM images of S/Rac-Br-MBABr (n = 2); statistic roughness of S/Rac-Br-MBABr (n = 2); TA spectra at selected time scales of S/Rac-Br-MBABr (n = 2); pump fluence-dependent normalized band-edge exciton relaxation kinetics of S/Rac-Br-MBABr (n = 2); the PL spectra of S/Rac-Br-MBABr (n = 1); the temperature-dependent full-width at half-maximum (fwhm) analysis of the absorption and PL spectra; phonon band structure and phonon density of states of S/Rac-Br-MBABr (n = 1); the calculation of the distortion degree of the intraoctahedron; crystal structures of S/Rac-X-MBABr (X = F, Cl, Br, 3Br); the electronic band structure and orbital projected partial density of states of S/Rac-Br-MBABr (n = 1); transmission spectra of the DBR mirror and Ag mirror; the ASE threshold of the quasi-2D perovskite film; statistical analysis of perovskite continuous wave lasing threshold (PDF)

AUTHOR INFORMATION

Corresponding Authors

Yuanhui Sun − *Suzhou National Laboratory, Suzhou 215123, China;* orcid.org/0000-0003-2981-1133; Email: sunyh@szlab.ac.cn

Beibei Xu − *State Key Laboratory of Extreme Photonics and Instrumentation, College of Optical Science and Engineering, Zhejiang University, Zhejiang, Hangzhou 310027, China;* orcid.org/0000-0003-2789-7973; Email: bbxu2019@zju.edu.cn

Authors

Zicheng Li − *State Key Laboratory of Extreme Photonics and Instrumentation, College of Optical Science and Engineering, Zhejiang University, Zhejiang, Hangzhou 310027, China;* orcid.org/0009-0007-4506-3450

Xinyu Duan − *State Key Laboratory of Extreme Photonics and Instrumentation, College of Optical Science and Engineering, Zhejiang University, Zhejiang, Hangzhou 310027, China*

Hanting Meng − *Beijing National Laboratory for Condensed Matter Physics, Laboratory of Soft Matter Physics, Institute of Physics, Chinese Academy of Sciences, Beijing 100190, China; University of Chinese Academy of Sciences, Beijing 100049, China*

Tao Man − *State Key Laboratory of Extreme Photonics and Instrumentation, College of Optical Science and Engineering, Zhejiang University, Zhejiang, Hangzhou 310027, China*

Nan Gong − *State Key Laboratory of Extreme Photonics and Instrumentation, College of Optical Science and Engineering, Zhejiang University, Zhejiang, Hangzhou 310027, China;* orcid.org/0000-0002-0140-8476

Lin-Han Li − *State Key Laboratory of Superlattices and Microstructures, Institute of Semiconductors, Chinese Academy of Sciences, Beijing 100083, China*

Zehui Zhou − *State Key Laboratory of Extreme Photonics and Instrumentation, College of Optical Science and Engineering, Zhejiang University, Zhejiang, Hangzhou 310027, China*

Can Wang − *Fujian Institute of Research on the Structure of Matter, Chinese Academy of Sciences, Fuzhou 350002, China*

Gongxun Bai − *Key Laboratory of Rare Earth Optoexcitonic Materials and Devices of Zhejiang Province, China Jiliang University, Hangzhou 310018, China;* orcid.org/0000-0002-4066-0359

Zhi Chen − *College of Materials Science and Engineering, Key Laboratory of Advanced Materials of Yunnan Province, Kunming University of Science and Technology, Kunming 650093, China*

Zhenhuang Su − *Shanghai Synchrotron Radiation Facility (SSRF), Shanghai Advanced Research Institute, Chinese Academy of Sciences, Shanghai 201204, P. R. China;* orcid.org/0000-0003-0026-2601

Xingyu Gao − *Shanghai Synchrotron Radiation Facility (SSRF), Shanghai Advanced Research Institute, Chinese Academy of Sciences, Shanghai 201204, P. R. China;* orcid.org/0000-0003-1477-0092

Xiaofeng Liu − *School of Materials Science and Engineering, Zhejiang University, Zhejiang, Hangzhou 310027, China;* orcid.org/0000-0003-2932-022X

Weidong Shen − *State Key Laboratory of Extreme Photonics and Instrumentation, College of Optical Science and Engineering, Zhejiang University, Zhejiang, Hangzhou 310027, China;* orcid.org/0000-0003-0978-6807

Wei Qin − *School of Physics, State Key Laboratory of Crystal Materials, Shandong University, Jinan 250100, China;* orcid.org/0000-0003-4579-0061

Peng Gao − *Fujian Institute of Research on the Structure of Matter, Chinese Academy of Sciences, Fuzhou 350002, China;* orcid.org/0000-0002-4963-2282

YuHuang Wang − *Department of Chemistry and Biochemistry, University of Maryland, College Park, Maryland 20742, United States;* orcid.org/0000-0002-5664-1849

Lijun Zhang − *State Key Laboratory of Integrated Optoexcitonics, College of Materials Science and Engineering, Jilin University, Changchun 130012, China;* orcid.org/0000-0002-6438-5486

Ping-Heng Tan − *State Key Laboratory of Superlattices and Microstructures, Institute of Semiconductors, Chinese Academy of Sciences, Beijing 100083, China;* orcid.org/0000-0001-6575-1516

Hailong Chen − *Beijing National Laboratory for Condensed Matter Physics, Laboratory of Soft Matter Physics, Institute of Physics, Chinese Academy of Sciences, Beijing 100190, China; University of Chinese Academy of Sciences, Beijing 100049, China;* orcid.org/0000-0002-3456-7836

Jianrong Qiu − *State Key Laboratory of Extreme Photonics and Instrumentation, College of Optical Science and Engineering, Zhejiang University, Zhejiang, Hangzhou 310027, China;* orcid.org/0000-0003-3148-2500

Complete contact information is available at: https://pubs.acs.org/10.1021/acsnano.5c18306

Author Contributions

B.X. and Z.L. conceived the idea. Z.L. synthesized the samples and prepared the laser device. Z.L. performed the optical characterizations with the help of X.D., T.M., N.G., and Z.Z. Z.L. performed AFM, PLQY, and SEM measurements. Y.S. and L.Z. carried out the theoretical calculations and analyzed the data. L.L. and P.T. helped with the Raman spectrum test. Z.S. and X.G. performed GIWAXS measurements and analyses. W.Q., H.M., and H.C. performed transient absorption and resonant impulsive Raman spectral characterizations. C.W. and P.G. helped to synthesize the partial materials. G.B., Z.C., X.L., Y.W., and W.S. participated in the discussion of experimental results. J.Q. and B.X. supervised the project. Z.L. and B.X.

https://doi.org/10.1021/acsnano.5c18306
ACS Nano 2026, 20, 9192−9204

wrote the manuscript. All authors have interpreted the findings, commented on the paper, and approved the final version.

Notes

The authors declare no competing financial interest.

■ ACKNOWLEDGMENTS

This work was financially supported in part by the National Science and Technology Major Project (Grant No. 2023ZD0120702), the National Natural Science Foundation of China (Grant No. 62375243), the Natural Science Foundation of Zhejiang Province (Grant No. LQ24B030001), the Fundamental Research Funds for the Central Universities (Grant No. 50672087), and the Basic Research Program of Jiangsu (No. BK20240391). This work was supported by the Open Research Fund of the State Key Laboratory of Extreme Photonics and instrumentation Zhejiang University. DFT computations were performed on Sugon HPC clusters equipped with HYGON C86 7285H 32-core processors (2.5 GHz).

■ REFERENCES

(1) Ma, D.; Lin, K.; Dong, Y.; Choubisa, H.; Proppe, A. H.; Wu, D.; Wang, Y. K.; Chen, B.; Li, P.; Fan, J. Z.; Yuan, F.; Johnston, A.; Liu, Y.; Kang, Y.; Lu, Z. H.; Wei, Z.; Sargent, E. H. Distribution Control Enables Efficient Reduced-Dimensional Perovskite LEDs. *Nature* **2021**, *599* (7886), 594−598.

(2) Qin, C.; Sandanayaka, A. S. D.; Zhao, C.; Matsushima, T.; Zhang, D.; Fujihara, T.; Adachi, C. Stable Room-Temperature Continuous-Wave Lasing in Quasi-2D Perovskite Films. *Nature* **2020**, *585* (7823), 53−57.

(3) Hailegnaw, B.; Demchyshyn, S.; Putz, C.; Lehner, L. E.; Mayr, F.; Schiller, D.; Pruckner, R.; Cobet, M.; Ziss, D.; Krieger, T. M.; Rastelli, A.; Sariciftci, N. S.; Scharber, M. C.; Kaltenbrunner, M. Flexible Quasi-2D Perovskite Solar Cells with High Specific Power and Improved Stability for Energy-Autonomous Drones. *Nat. Energy* **2024**, *9* (6), 677−690.

(4) Min, L.; Tian, W.; Cao, F.; Guo, J.; Li, L. 2D Ruddlesden-Popper Perovskite with Ordered Phase Distribution for High-Performance Self-Powered Photodetectors. *Adv. Mater.* **2021**, *33* (35), No. e2101714.

(5) Man, T.; Gong, N.; Li, Z.; Duan, X.; Xu, B.; Song, Z.; Lin, X.; Tan, D.; Liu, X.; Qiu, J. In Situ Passivation of Two-Dimensional Perovskites by External Electric Field. *Adv. Opt. Mater.* **2023**, *11* (23), 2300969.

(6) Zhou, N.; Zhang, Y.; Huang, Z.; Guo, Z.; Zhu, C.; He, J.; Chen, Q.; Sun, W.; Zhou, H. Mobile Media Promotes Orientation of 2D/3D Hybrid Lead Halide Perovskite for Efficient Solar Cells. *ACS Nano* **2021**, *15* (5), 8350−8362.

(7) Zhang, Q.; Zhang, D.; Cao, B.; Poddar, S.; Mo, X.; Fan, Z.Improving the Operational Lifetime of Metal-Halide Perovskite Light-Emitting Diodes with Dimension Control and Ligand Engineering. *ACS Nano*; American Chemical Society March 26, 2024; pp 8557−8570.

(8) Chen, X.; Feng, W.; Fang, Y.; Li, Q.; Huang, Y. H.; Chang, X.; Yao, C.; Shen, Y.; Liu, G.; Yang, S.; Wang, X. D.; Yuan, M.; Wu, W. Q. Improved Conductivity of 2D Perovskite Capping Layer for Realizing High-Performance 3D/2D Heterostructured Hole Transport Layer-Free Perovskite Photovoltaics. *ACS Nano* **2025**, *19* (4), 4299−4308.

(9) Wu, C.; Wu, T.; Yang, Y.; McLeod, J. A.; Wang, Y.; Zou, Y.; Zhai, T.; Li, J.; Ban, M.; Song, T.; Gao, X.; Duhm, S.; Sirringhaus, H.; Sun, B. Alternative Type Two-Dimensional-Three-Dimensional Lead Halide Perovskite with Inorganic Sodium Ions as a Spacer for High-Performance Light-Emitting Diodes. *ACS Nano* **2019**, *13* (2), 1645−1654.

(10) Weidman, M. C.; Seitz, M.; Stranks, S. D.; Tisdale, W. A. Highly Tunable Colloidal Perovskite Nanoplatelets through Variable Cation, Metal, and Halide Composition. *ACS Nano* **2016**, *10* (8), 7830−7839.

(11) Cheng, Y.; Wan, H.; Sargent, E. H.; Ma, D. Reduced-Dimensional Perovskites: Quantum Well Thickness Distribution and Optoelectronic Properties. *Adv. Mater.* **2024**, *37* (25), 2410633.

(12) Gu, H.; Xia, J.; Liang, C.; Chen, Y.; Huang, W.; Xing, G. Phase-Pure Two-Dimensional Layered Perovskite Thin Films. *Nat. Rev. Mater.* **2023**, *8* (8), 533−551.

(13) Zhang, Y.; Abdi-Jalebi, M.; Larson, B. W.; Zhang, F. What Matters for the Charge Transport of 2D Perovskites? *Adv. Mater.* **2024**, *36* (31), No. e2404517.

(14) Liang, Y.; Gao, X.; Li, C.; Yang, C.; Cai, X. H.; Gong, Y.; Li, M.; Tang, K. K.; Song, J.; Deng, X.; Han, X.; Yue, S.; Zhao, X.; Xing, G.; Wang, M.; Gao, P.; Wu, B.; Liu, X.; Zhang, Q. Enhanced Interfacial Exciton Transport in Mixed 2D/3D Perovskites Approaching Bulk 3D Counterparts. *ACS Nano* **2025**, *19* (19), 18833−18842.

(15) Chen, C.; Gao, L.; Gao, W.; Ge, C.; Du, X.; Li, Z.; Yang, Y.; Niu, G.; Tang, J. Circularly Polarized Light Detection Using Chiral Hybrid Perovskite. *Nat. Commun.* **2019**, *10* (1), 1927.

(16) Long, G.; Jiang, C.; Sabatini, R.; Yang, Z.; Wei, M.; Quan, L. N.; Liang, Q.; Rasmita, A.; Askerka, M.; Walters, G.; Gong, X.; Xing, J.; Wen, X.; Quintero-Bermudez, R.; Yuan, H.; Xing, G.; Wang, X. R.; Song, D.; Voznyy, O.; Zhang, M.; Hoogland, S.; Gao, W.; Xiong, Q.; Sargent, E. H. Spin Control in Reduced-Dimensional Chiral Perovskites. *Nat. Photonics* **2018**, *12* (9), 528−533.

(17) Yuan, C.; Li, X.; Semin, S.; Feng, Y.; Rasing, T.; Xu, J. Chiral Lead Halide Perovskite Nanowires for Second-Order Nonlinear Optics. *Nano Lett.* **2018**, *18* (9), 5411−5417.

(18) Ai, Y.; Chen, X. G.; Shi, P. P.; Tang, Y. Y.; Li, P. F.; Liao, W. Q.; Xiong, R. G. Fluorine Substitution Induced High Tc of Enantiomeric Perovskite Ferroelectrics: (R) - And (S) −3-(Fluoropyrrolidinium)$MnCl_3$. *J. Am. Chem. Soc.* **2019**, *141* (10), 4474−4479.

(19) Kim, K.; Vetter, E.; Yan, L.; Yang, C.; Wang, Z.; Sun, R.; Yang, Y.; Comstock, A. H.; Li, X.; Zhou, J.; Zhang, L.; You, W.; Sun, D.; Liu, J. Chiral-Phonon-Activated Spin Seebeck Effect. *Nat. Mater.* **2023**, *22* (3), 322−328.

(20) Sun, R.; Park, K. S.; Comstock, A. H.; McConnell, A.; Chen, Y. C.; Zhang, P.; Beratan, D.; You, W.; Hoffmann, A.; Yu, Z. G.; Diao, Y.; Sun, D. Inverse Chirality-Induced Spin Selectivity Effect in Chiral Assemblies of π-Conjugated Polymers. *Nat. Mater.* **2024**, *23* (6), 782−789.

(21) Li, P.-F.; Liao, W.-Q.; Tang, Y.-Y.; Qiao, W.; Zhao, D.; Ai, Y.; Yao, Y.-F.; Xiong, R.-G. Organic Enantiomeric High- T_c Ferroelectrics. *Proc. Natl. Acad. Sci. U. S. A.* **2019**, *116* (13), 5878−5885.

(22) Peng, H.; Qi, J. C.; Liu, Y. S.; Zhang, J. M.; Liao, W. Q.; Xiong, R. G. Homochirality in Ferroelectrochemistry. *Chin. J. Chem.* **2024**, *42* (10), 1133−1144.

(23) Gao, M.; Wang, Z.; Ren, S.; Hao, X.; Qin, W. Organic Chiral Ferromagnets with Strong Spin-Chiroptical Interactions. *Cell Rep. Phys. Sci.* **2021**, *2* (6), No. 100442.

(24) Nandkishore, R.; Levitov, L. S.; Chubukov, A. V. Chiral Superconductivity from Repulsive Interactions in Doped Graphene. *Nat. Phys.* **2012**, *8* (2), 158−163.

(25) Liu, Y.; Xiao, J.; Koo, J.; Yan, B. Chirality-Driven Topological Electronic Structure of DNA-like Materials. *Nat. Mater.* **2021**, *20* (5), 638−644.

(26) Li, H.; Sun, Z.; Liu, Y.; Xing, Y.; Gao, J.; Shi, A.; Yu, Y.; Long, J.; Song, D.; Jin, C.; McKee, M. D.; Ma, J.; Jiang, W. Chiral Gypsum with High-performance Mechanical Properties Induced by Self-assembly of Chiral Amino Acid on an Amorphous Mineral. *SmartMat* **2024**, *5* (6), No. e1302.

(27) Jana, M. K.; Song, R.; Liu, H.; Khanal, D. R.; Janke, S. M.; Zhao, R.; Liu, C.; Valy Vardeny, Z.; Blum, V.; Mitzi, D. B. Organic-to-Inorganic Structural Chirality Transfer in a 2D Hybrid Perovskite and Impact on Rashba-Dresselhaus Spin-Orbit Coupling. *Nat. Commun.* **2020**, *11* (1), 4699.

https://doi.org/10.1021/acsnano.5c18306
ACS Nano 2026, 20, 9192−9204

(28) Lu, H.; Xiao, C.; Song, R.; Li, T.; Maughan, A. E.; Levin, A.; Brunecky, R.; Berry, J. J.; Mitzi, D. B.; Blum, V.; Beard, M. C. Highly Distorted Chiral Two-Dimensional Tin Iodide Perovskites for Spin Polarized Charge Transport. *J. Am. Chem. Soc.* **2020**, *142* (30), 13030−13040.
(29) Ma, J.; Fang, C.; Chen, C.; Jin, L.; Wang, J.; Wang, S.; Tang, J.; Li, D. Chiral 2D Perovskites with a High Degree of Circularly Polarized Photoluminescence. *ACS Nano* **2019**, *13* (3), 3659−3665.
(30) Liu, S.; Kepenekian, M.; Bodnar, S.; Feldmann, S.; Heindl, M. W.; Fehn, N.; Zerhoch, J.; Shcherbakov, A.; Pöthig, A.; Li, Y.; Paetzold, U. W.; Kartouzian, A.; Sharp, I. D.; Katan, C.; Even, J.; Deschler, F. Bright Circularly Polarized Photoluminescence in Chiral Layered Hybrid Lead-Halide Perovskites. *Sci. Adv.* **2023**, *9* (35), No. eadh5083.
(31) Lu, H.; Wang, J.; Xiao, C.; Pan, X.; Chen, X.; Brunecky, R.; Berry, J. J.; Zhu, K.; Beard, M. C.; Vardeny, Z. V. Spin-Dependent Charge Transport through 2D Chiral Hybrid Lead-Iodide Perovskites. *Sci. Adv.* **2019**, *5* (12), No. eaay0571.
(32) Kong, L.; Zhang, X.; Li, Y.; Wang, H.; Jiang, Y.; Wang, S.; You, M.; Zhang, C.; Zhang, T.; Kershaw, S. V.; Zheng, W.; Yang, Y.; Lin, Q.; Yuan, M.; Rogach, A. L.; Yang, X. Smoothing the Energy Transfer Pathway in Quasi-2D Perovskite Films Using Methanesulfonate Leads to Highly Efficient Light-Emitting Devices. *Nat. Commun.* **2021**, *12* (1), 1246.
(33) Yao, J.; Wang, Z.; Huang, Y.; Xue, J.; Zhang, D.; Chen, J.; Chen, X.; Dong, S. C.; Lu, H. Efficient Green Spin Light-Emitting Diodes Enabled by Ultrafast Energy- and Spin-Funneling in Chiral Perovskites. *J. Am. Chem. Soc.* **2024**, *146* (20), 14157−14165.
(34) Zhang, T.; Zhou, C.; Feng, X.; Dong, N.; Chen, H.; Chen, X.; Zhang, L.; Lin, J.; Wang, J. Regulation of the Luminescence Mechanism of Two-Dimensional Tin Halide Perovskites. *Nat. Commun.* **2022**, *13* (1), 60.
(35) Wang, X.; Jin, L.; Sergeev, A.; Liu, W.; Gu, S.; Li, N.; Fan, K.; Chen, S. c.; Wong, K. S.; Sun, X.; Zhao, N. Quasi-2D Dion-Jacobson Phase Perovskites as a Promising Material Platform for Stable and High-Performance Lasers. *Sci. Adv.* **2023**, *9* (43), No. eadj3476.
(36) Lai, R.; Yang, Z.; Zhi, C.; Cao, X.; Li, Z.; Di, D.; Yang, Y. Transient Suppression of Carrier Mobility Due to Hot Optical Phonons in Lead Bromide Perovskites. *J. Phys. Chem. Lett.* **2022**, *13* (24), 5488−5494.
(37) Wright, A. D.; Verdi, C.; Milot, R. L.; Eperon, G. E.; Pérez-Osorio, M. A.; Snaith, H. J.; Giustino, F.; Johnston, M. B.; Herz, L. M. Electron−Phonon Coupling in Hybrid Lead Halide Perovskites. *Nat. Commun.* **2016**, *7* (1), 11755.
(38) Rudin, S.; Reinecke, T. L.; Segall, B. Temperature-Dependent Exciton Linewidths in Semiconductors. *Phys. Rev. B* **1990**, *42* (17), 11218−11231.
(39) Carreras, A.; Togo, A.; Tanaka, I. DynaPhoPy: A Code for Extracting Phonon Quasiparticles from Molecular Dynamics Simulations. *Comput. Phys. Commun.* **2017**, *221*, 221−234.
(40) Tong, W. Y.; Gong, S. J.; Wan, X.; Duan, C. G. Concepts of Ferrovalley Material and Anomalous Valley Hall Effect. *Nat. Commun.* **2016**, *7* (1), 13612.
(41) Yang, Y.; Ostrowski, D. P.; France, R. M.; Zhu, K.; Van De Lagemaat, J.; Luther, J. M.; Beard, M. C. Observation of a Hot-Phonon Bottleneck in Lead-Iodide Perovskites. *Nat. Photonics* **2016**, *10* (1), 53−59.
(42) Fu, J.; Xu, Q.; Han, G.; Wu, B.; Huan, C. H. A.; Leek, M. L.; Sum, T. C. Hot Carrier Cooling Mechanisms in Halide Perovskites. *Nat. Commun.* **2017**, *8* (1), 1300.
(43) Mitzi, D. B.; Dimitrakopoulos, C. D.; Kosbar, L. L. Structurally Tailored Organic-Inorganic Perovskites: Optical Properties and Solution-Processed Channel Materials for Thin-Film Transistors. *Chem. Mater.* **2001**, *13* (10), 3728−3740.
(44) Jana, M. K.; Song, R.; Xie, Y.; Zhao, R.; Sercel, P. C.; Blum, V.; Mitzi, D. B. Structural Descriptor for Enhanced Spin-Splitting in 2D Hybrid Perovskites. *Nat. Commun.* **2021**, *12* (1), 4982.
(45) Song, J.; Ghosh, S.; Deng, X.; Li, C.; Shang, Q.; Liu, X.; Wang, Y.; Gao, X.; Yang, W.; Wang, X.; Zhao, Q.; Shi, K.; Gao, P.; Xing, G.; Xiong, Q.; Zhang, Q. Room-Temperature Continuous-Wave Pumped Exciton Polariton Condensation in a Perovskite Microcavity. *Sci. Adv.* **2025**, *11* (5), 1−10.
(46) Kresse, G.; Furthmüller, J. Efficient Iterative Schemes for *Ab Initio* Total-Energy Calculations Using a Plane-Wave Basis Set. *Phys. Rev. B* **1996**, *54* (16), 11169−11186.
(47) Kresse, G.; Joubert, D. From Ultrasoft Pseudopotentials to the Projector Augmented-Wave Method. *Phys. Rev. B* **1999**, *59* (3), 1758−1775.
(48) Blöchl, P. E. Projector Augmented-Wave Method. *Phys. Rev. B* **1994**, *50* (24), 17953−17979.
(49) Perdew, J. P.; Burke, K.; Ernzerhof, M. Generalized Gradient Approximation Made Simple. *Phys. Rev. Lett.* **1996**, *77* (18), 3865−3868.
(50) Klimeš, J.; Bowler, D. R.; Michaelides, A. Van Der Waals Density Functionals Applied to Solids. *Phys. Rev. B Condens. Matter Mater. Phys.* **2011**, *83* (19), No. 195131.
(51) Togo, A.; Tanaka, I. First Principles Phonon Calculations in Materials Science. *Scr. Mater.* **2015**, *108*, 1−5.

https://doi.org/10.1021/acsnano.5c18306
ACS Nano 2026, 20, 9192−9204

Abnormal Chiral Coupling for Efficient and Stable Reduced-dimensional Perovskite Emitters

Zicheng Li[1], Xinyu Duan[1], Hanting Meng[3], Tao Man[1], Nan Gong[1], Lin-Han Li[4], Zehui Zhou[1], Can Wang[11], Gongxun Bai[10], Zhi Chen[12], Zhenhuang Su[9], Xingyu Gao[9], Xiaofeng Liu[8], Weidong Shen[1], Wei Qin[7], Peng Gao[11], YuHuang Wang[6], Lijun Zhang[5], Ping-Heng Tan[4], Hailong Chen[3], Jianrong Qiu[1], Yuanhui Sun[2]*, Beibei Xu[1]*

[1]State Key Laboratory of Extreme Photonics and Instrumentation, College of Optical Science and Engineering, Zhejiang University, Hangzhou, Zhejiang 310027, China

[2]Suzhou National Laboratory, Suzhou 215123, China

[3]Beijing National Laboratory for Condensed Matter Physics, Laboratory of Soft Matter Physics, Institute of Physics, Chinese Academy of Sciences, Beijing 100190, China; University of Chinese Academy of Sciences, Beijing 100049, China.

[4]State Key Laboratory of Superlattices and Microstructures, Institute of Semiconductors, Chinese Academy of Sciences, Beijing 100083, China

[5]State Key Laboratory of Integrated Optoelectronics, College of Materials Science and Engineering, Jilin University, Changchun 130012, China

[6]Department of Chemistry and Biochemistry, University of Maryland, College Park, Maryland 20742, United States

[7] School of Physics, State Key Laboratory of Crystal Materials, Shandong University, Jinan 250100, China

[8]School of Materials Science and Engineering, Zhejiang University, Hangzhou, Zhejiang 310027, China

[9]Shanghai Synchrotron Radiation Facility (SSRF), Shanghai Advanced Research Institute, Chinese Academy of Sciences 239 Zhang heng Road, Shanghai 201204, P. R. China

[10]Key Laboratory of Rare Earth Optoelectronic Materials and Devices of Zhejiang Province, China Jiliang University, Hangzhou 310018, China

[11]Fujian Institute of Research on the Structure of Matter, Chinese Academy of Sciences, Fuzhou 350002, China

[12]College of Materials Science and Engineering, Key Laboratory of Advanced Materials of Yunnan Province, Kunming University of Science and Technology, Kunming 650093,

China.

E-mail: bbxu2019@zju.edu.cn; E-mail: sunyh@szlab.ac.cn

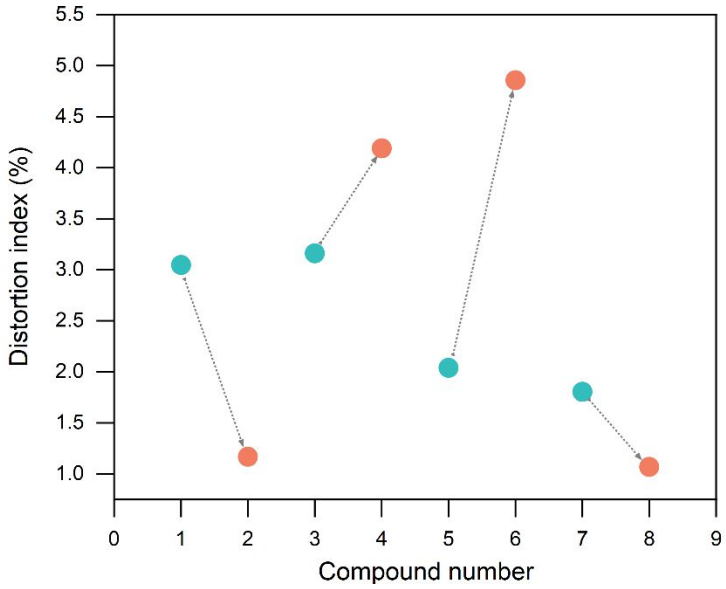

Figure. S1 Distortion index for perovskite structures resolved in this study (1–8).

Optical properties of perovskite film

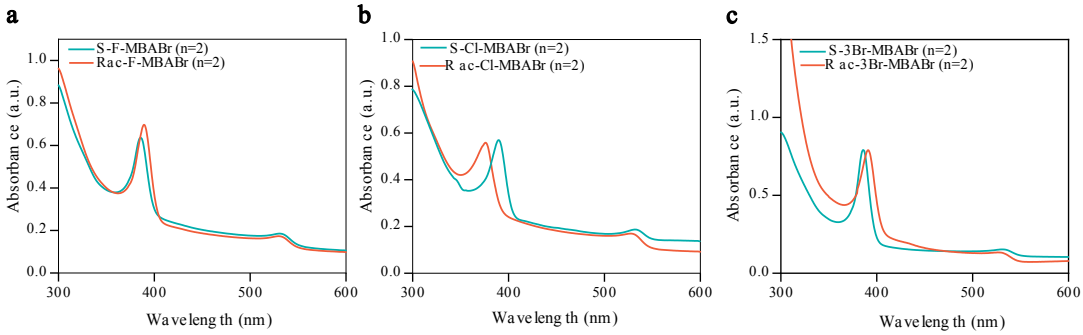

Figure. S2 The optical absorption spectra of S/Rac-F-MBA (n=2), S/Rac-Cl-MBA (n=2) and S/Rac-3Br-MBA (n=2) film.

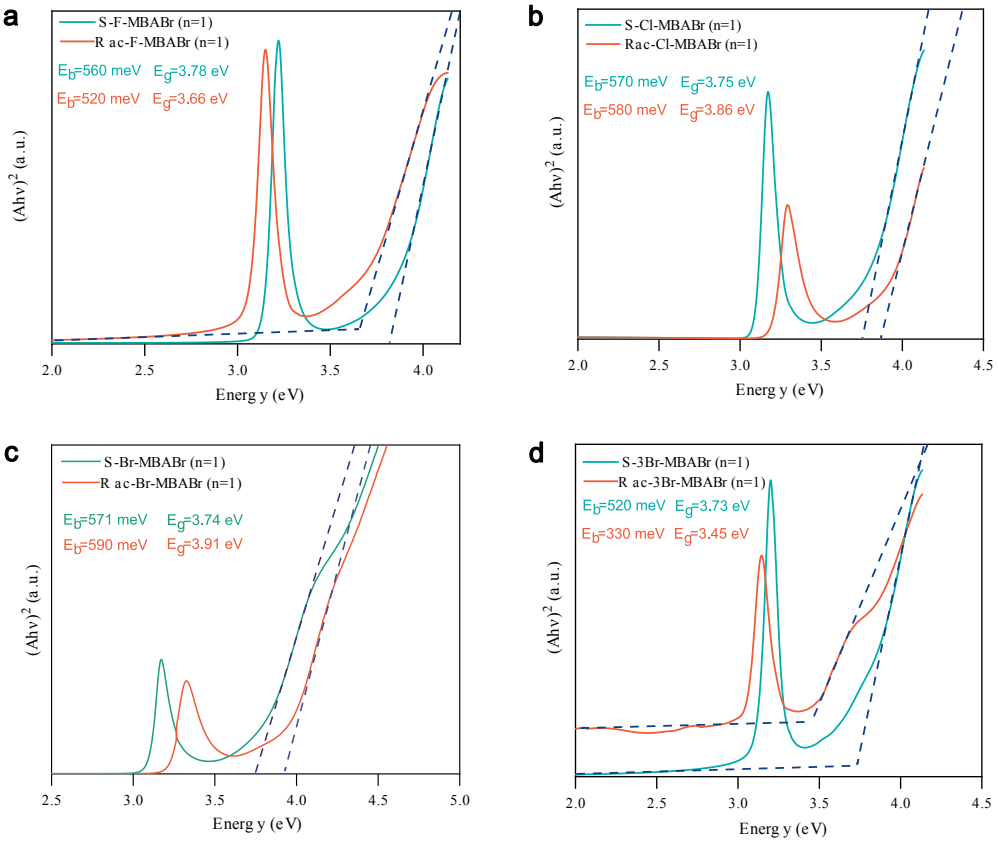

Figure. S3 The optical absorption spectra of S/Rac-X-MBA (n=1, X= F, Cl, Br, 3Br) film. The calculated band gap (E_g) and exciton binding energy (E_b) are exhibited.

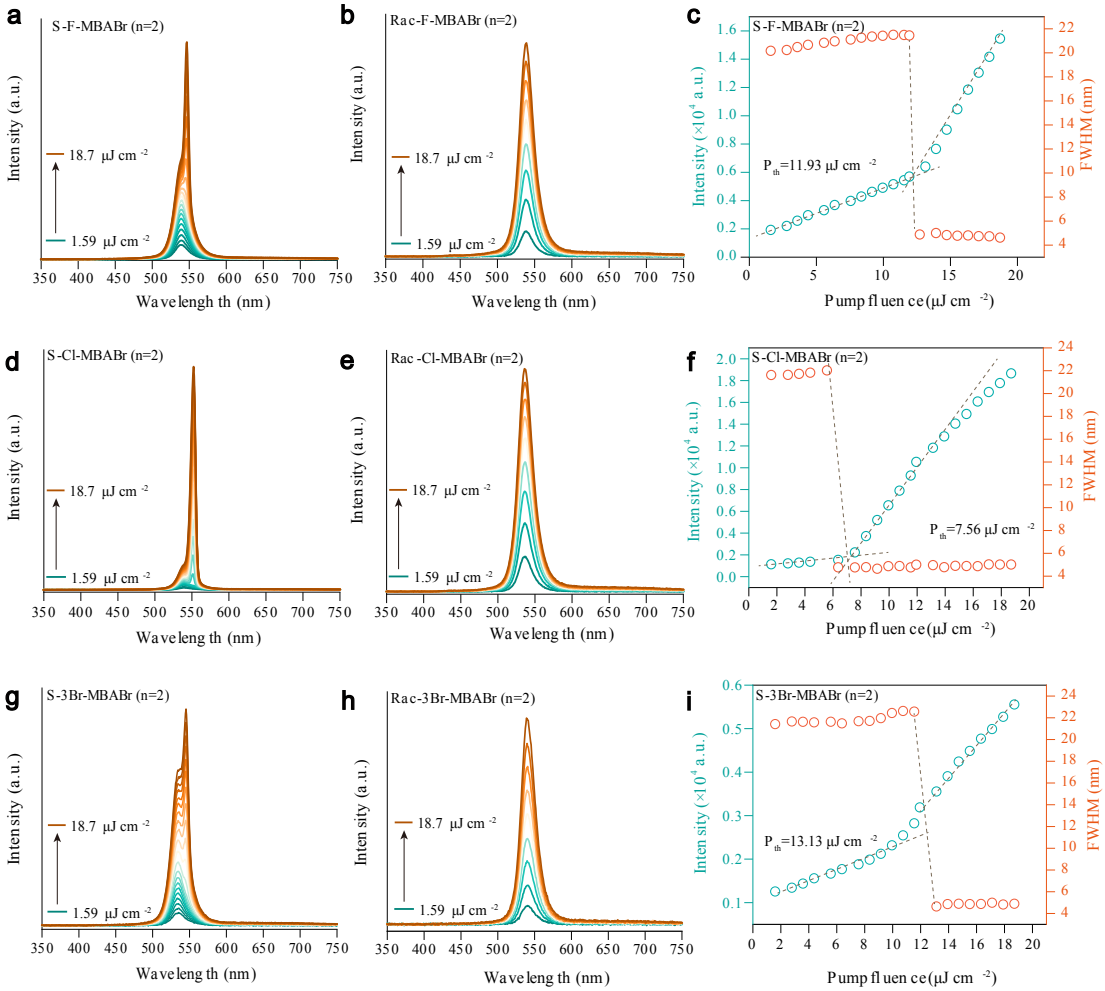

Figure. S4 Pump-fluence dependent emission spectra of (a) S-F-MBABr (n=2); (b) Rac-F-MBABr (n=2); (d) S-Cl-MBABr (n=2); (e) Rac-Cl-MBABr (n=2); (g) S-3Br-MBABr (n=2); (h) Rac-3Br-MBABr (n=2); Pump fluence dependent PL intensities and the full width at half maximum (FWHM) change of (c) S-F-MBABr (n=2) ; (f) S-Cl-MBABr (n=2); (i) S-3Br-MBABr (n=2)

Structure and excited state dynamics of perovskite film

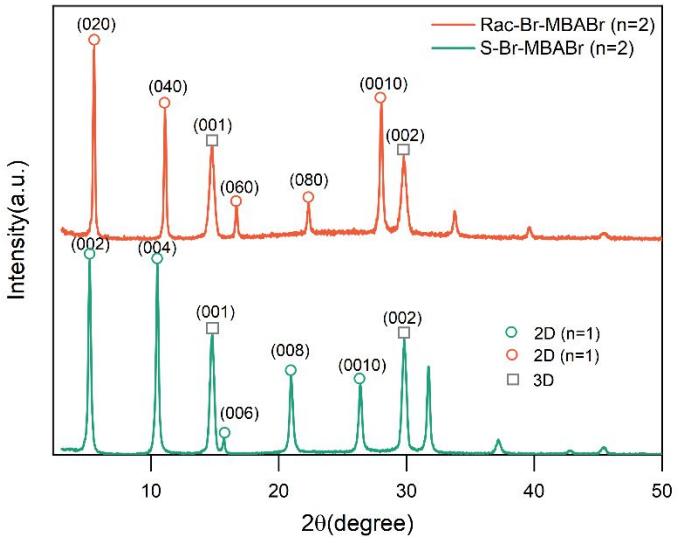

Figure. S5 Crystallographic orientation characterization of chiral S-Br-MBABr (n=2) and achiral Rac-Br-MBABr (n=2) film: 1D XRD patterns.

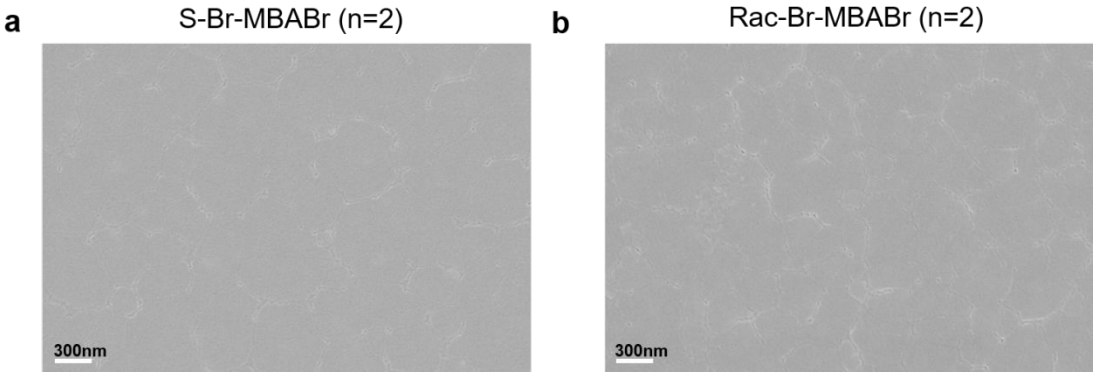

Figure. S6 SEM images of chiral S-Br-MBABr (n=2) (a) and achiral Rac-Br-MBABr (n=2) film (b).

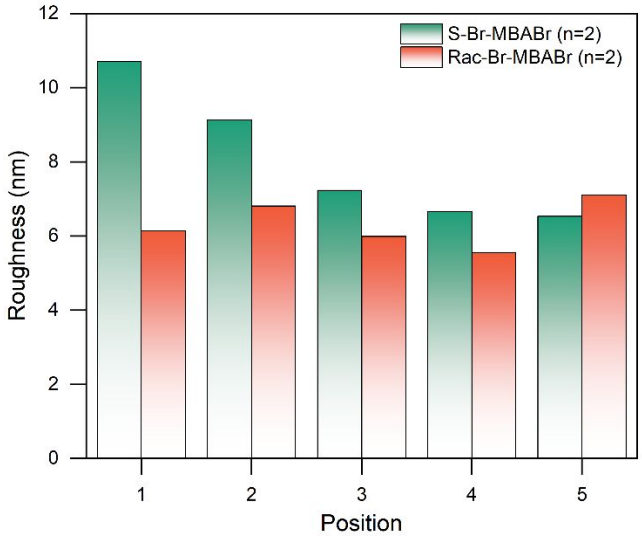

Figure. S7 Statistic roughness of chiral S-Br-MBABr (n=2) and achiral Rac-Br-MBABr (n=2) film in different region.

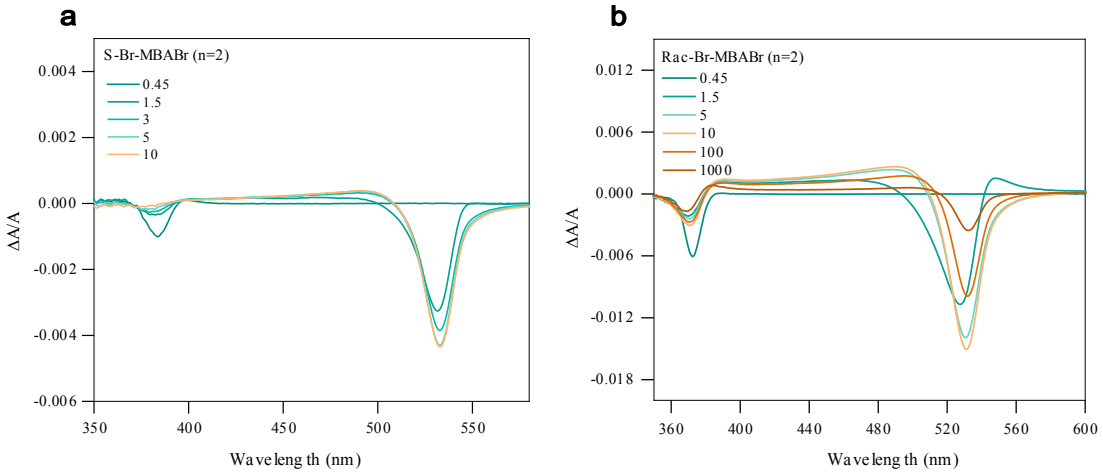

Figure. S8 (a) TA spectra at selected timescales of chiral S-Br-MBABr (n=2) and (b) achiral Rac-Br-MBABr (n=2). The time unit in the up-left inset is ps.

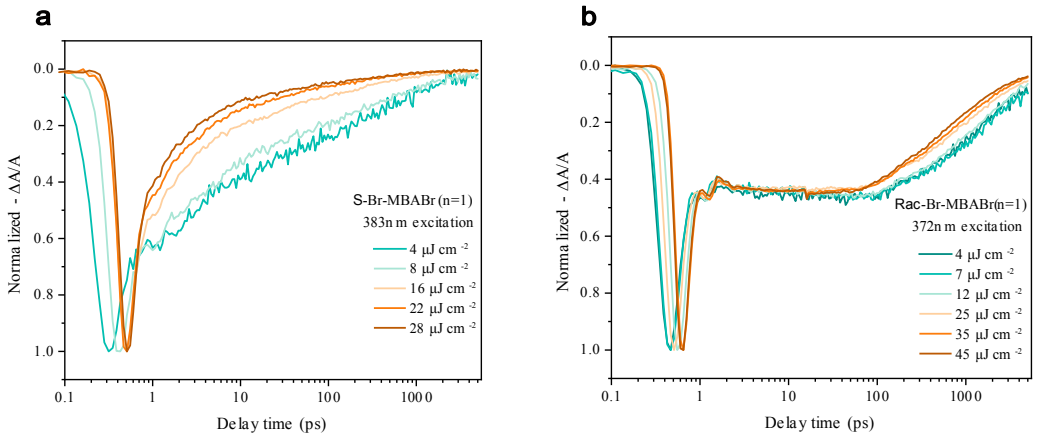

Figure. S9 Pump fluence-dependent normalized band-edge exciton relaxation kinetics of

(a) chiral S-Br-MBABr (n=1) and (b) achiral Rac-Br-MBABr (n=1).

We hypothesize that the disparity in energy/excited state transfer kinetics could be attributed to a greater prevalence of defect sites in the achiral 2D phase, which trap charge carriers, thereby resulting in diminished transfer efficiency. As shown in Figure. S9, we conducted pump fluence-dependent TA spectra to demonstrate the hypothesize, relevant analysis is given below.

For both pure 2D perovskite films at low excitation fluence, a slow decay dynamics process is exhibited, but the achiral sample occur at a flat and almost changeless region during 1-100 ps, followed by gradually decay. Concerning excited-state transfer for achiral RDPs sample (Figure. 3d), charge trapping from pure 2D (n=1) phase can be identified as a sudden decrease in the TA kinetics immediately after the signal build-up which is clearly visible at the low excitation levels of the shorter wavelength excitation (370 nm), followed by a process of relaxedly decrease and steeply decrease at higher fluxes (Figure. S9b) once the number of excited carriers fill trap density. Whereas, the signal of chiral 2D perovskites demonstrate a sustained reduction trend without flat region under low-energy excitation, with an acceleration in carrier decay rate as pump energy increases (Figure. S9a). This phenomenon suggests that chiral perovskites possess a lower density of defect states, preventing the trapping of carriers by defect states.

The conclusions drawn from transient absorption could be explained more cautiously. The slower decay in the racemic film is interpreted as a result of trap states. This is possible, but other effects such as self-trapped excitons or stronger exciton-phonon coupling could contribute. It would be helpful to present fitted decay components with uncertainties, or to provide additional support from time-resolved PL or power-dependent PL. A clearer justification would strengthen the cause-and-effect relationship proposed in the paper.

The significantly different dynamics likely result from a combination of several factors. First, stronger exciton-phonon coupling (Figure. 4, Table S2) may promote the localization of excitons into self-trapped exciton (STE) states, thereby slowing down energy delocalization and inter-well transport. Second, a higher concentration of defect sites in the achiral 2D phase (Figure. S9 and related analysis) may act as traps for charge carriers, further reducing transfer efficiency. We consulted relevant literature (e.g., *Chem. Rev.* 2023, 123, 8154-8231; Chem. Rev. 2019, 119, 3104−3139; J. Am. Chem. Soc. 2015, 137, 2089−2096) and combined it with our data for the following analysis: Time scale of self-trapped excitons (STE): In two-dimensional/three-dimensional lead halide perovskites, exciton self-trapping (forming STE) is typically an ultrafast process (<1 ps to a few picoseconds)[1] because it involves strong coupling between carriers and lattice distortions. Once formed, the recombination lifetime of STE (especially radiative recombination) can vary from tens of picoseconds to several nanoseconds, depending on the specific system and environment. However, the key points are: i) STE formation itself is extremely fast and should manifest within the first few picoseconds after excitation; ii) In TA spectra, STE typically exhibits a characteristic, redshifted, broadened Photobleaching, which differs from the band-edge exciton ground-state bleach (GSB) signal[2]. In Figure 3d, the GSB signal of the n=1 phase in the achiral sample shows a gradually decreasing trend within the 2–10 ps time window. This time scale is too slow for STE formation (which should already be complete) but is reasonable for the slow trapping of carriers by deep defect states. More

importantly, we did not observe a significant, time-evolving new characteristic peak in this region (~400–700 nm). Therefore, while the presence of a small amount of STE cannot be completely ruled out, the shape and kinetics of our TA data do not support STE as the dominant mechanism responsible for the signal decay between 2–10 ps.

Time scale of exciton-phonon coupling: Energy relaxation due to strong exciton-phonon coupling (hot carrier cooling) also primarily occurs on an ultrafast time scale from the first few hundred femtoseconds to a few picoseconds (e.g., *Nat. Mater.* 23, 937–943 (2024); *Nat. Commun.* 6, 8420 (2015)). It mainly affects the initial energy distribution and thermalization of carriers, rather than dominating the decay kinetics of exciton population on picosecond to nanosecond time scales. The slow decay observed in Figure 3d, which persists for hundreds of picoseconds after 2 ps, occurs on a time scale far exceeding that of typical hot carrier cooling and phonon scattering processes. Thus, strong exciton-phonon coupling is more likely to be one of the causes of initial exciton energy loss (affecting PLQY), but is unlikely to be the dominant factor determining the long-term decay dynamics after 2 ps.

Therefore, we conclude that the higher concentration of defect states in the achiral film, acting as effective non-radiative recombination centers and energy traps, is a primary factor leading to its inefficient EST, prolonged exciton lifetime (localization), and ultimately weakened ASE performance. The chiral coupling effect significantly reduces defect density by enhancing structural order, thereby optimizing the excited-state transfer pathways.

Electron-phonon interaction dynamics

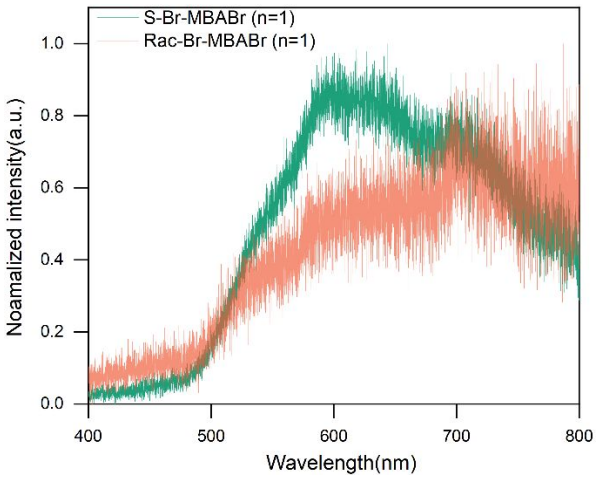

Figure. S10 The PL spectra for chiral S-Br-MBABr (n=1) (green) and achiral Rac-Br-MBABr (n=1) (brown) 2D perovskite film.

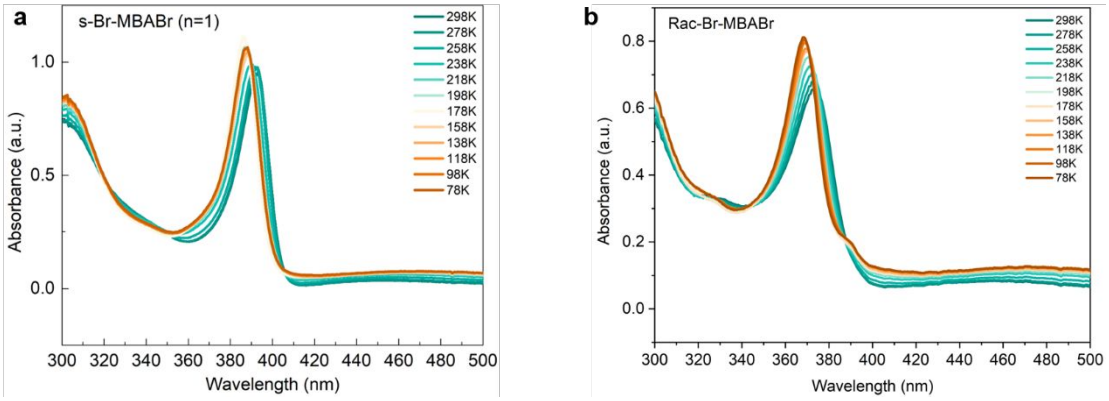

Figure. S11 The temperature-dependent full-width at half-maximum (FWHM) analysis of the absorption spectra (a) for S-Br-MBABr (n=1) and (b) Rac-Br-MBABr (n=1).

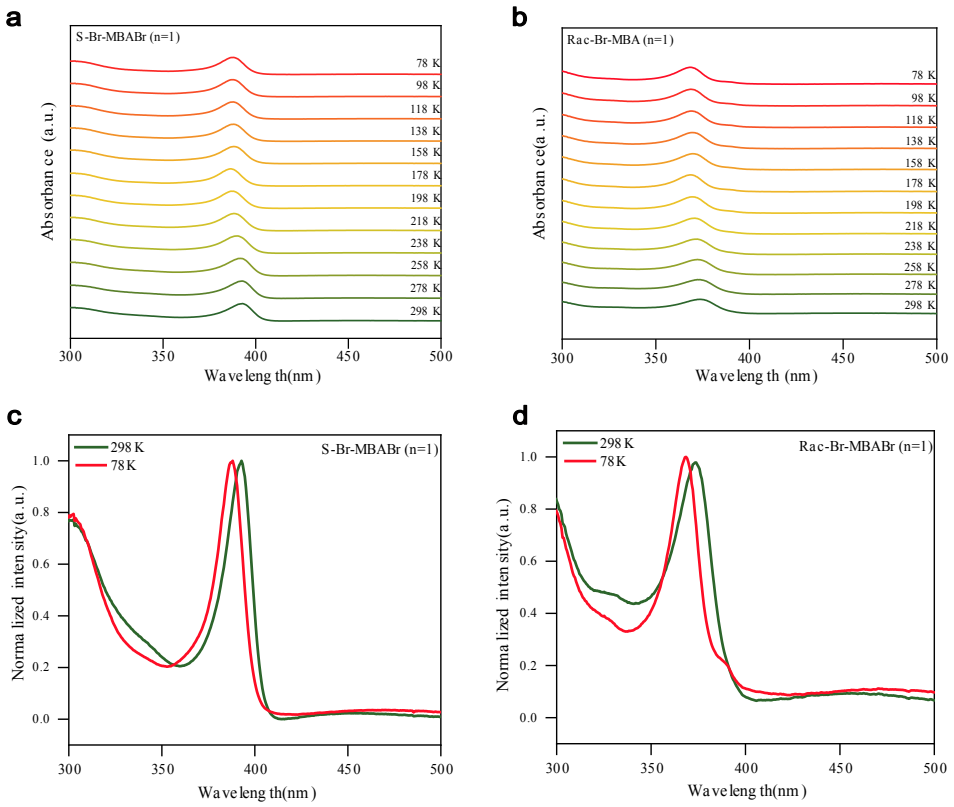

Figure. S12 Temperature dependent full-width at half-maximum (FWHM) analysis of the absorption spectra (a,c) for S-Br-MBABr (n=1) and (b, d) Rac-Br-MBABr (n=1).

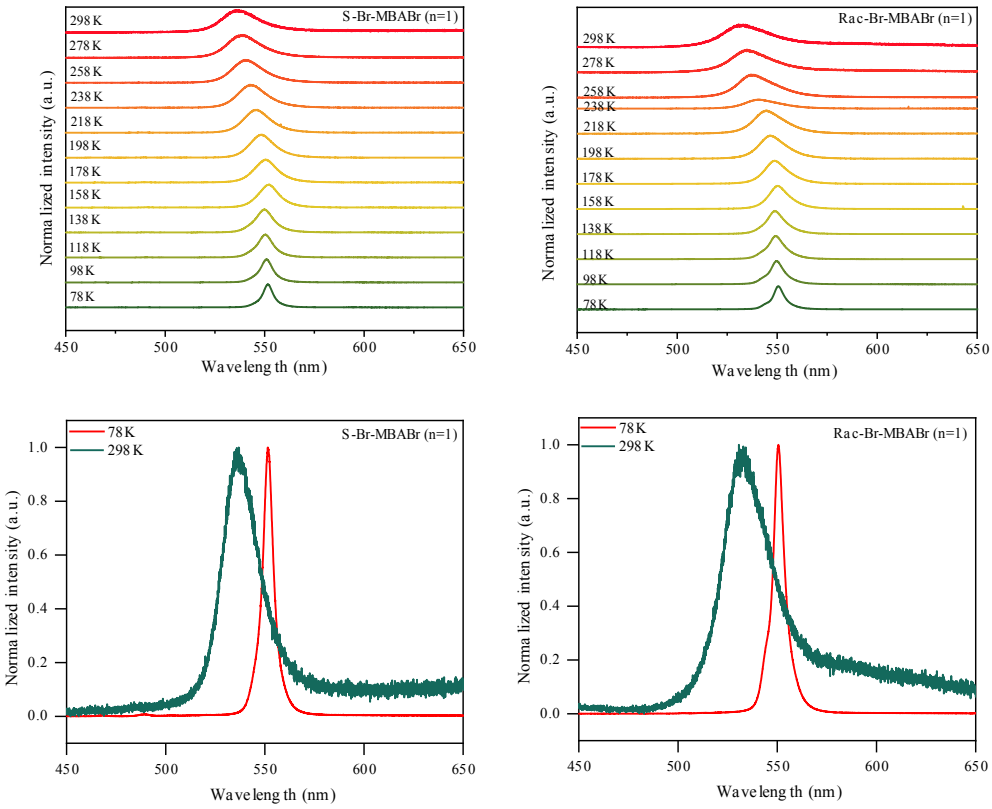

Figure. S13 The temperature-dependent full-width at half-maximum (FWHM) analysis of

the luminescence spectra (a, c) for S-Br-MBABr (n=2) and (b, d) Rac-Br-MBABr (n=2). The exciton absorption peak exhibits blueshifts from 298 to 158 K in the n = 1 phase for chiral and achiral perovskite, followed by a redshift due to structural phase transition at lower temperatures (Figure. S11-S12)[3]. The PL peak exhibits redshifts from 298 to 158 K in the n = 1 phase for chiral and achiral perovskite, followed by a blueshift (Figure. S13).

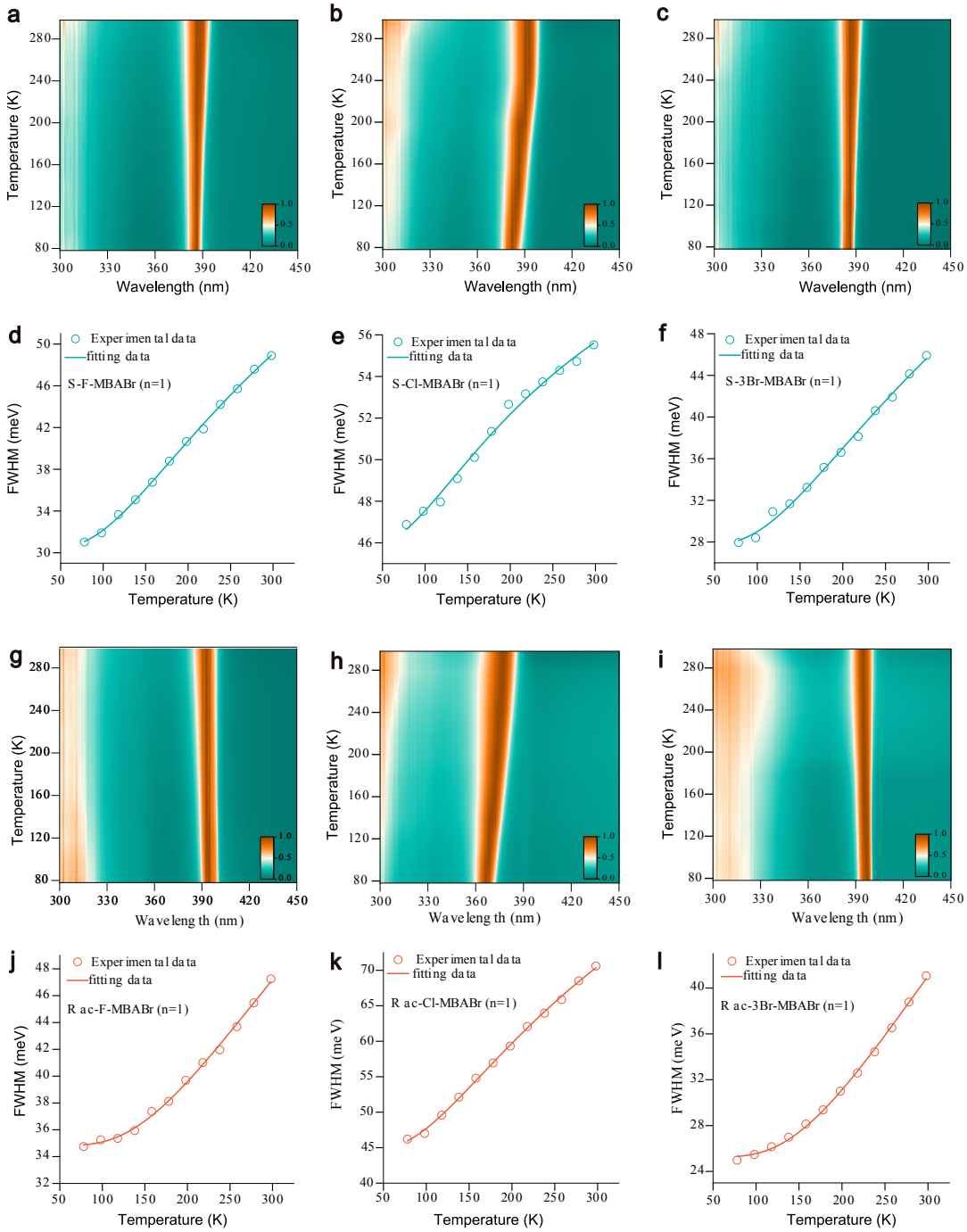

Figure. S14 Contour map of the temperature-dependent normalized steady-state absorption spectra of (a) S-F-MBABr (n=1), (b) S-Cl-MBABr (n=1) (n=1), (c) S-3Br-MBABr (n=1), (g) Rac-F-MBABr (n=1), (h) Rac -Cl-MBABr (n=1) (n=1), (i) Rac -3Br-MBABr (n=1) from 298 to 78 K with 20 K intervals; Temperature-dependent FWHM for the absorption

spectra of (d) S-F-MBABr (n=1), (e) S-Cl-MBABr (n=1) (n=1), (f) S-3Br-MBABr (n=1), (j) Rac-F-MBABr (n=1), (k) Rac -Cl-MBABr (n=1) (n=1), (l) Rac -3Br-MBABr (n=1).

Supplementary Note 1. exciton-phonon coupling model

The broadening of temperature dependent PL is in connection with the interference of lattice scattering with electron motion in various ways. The comprehensive broadening PL can be described by the sum of broadening contributions, as following Equation 1[3]:

$$\Gamma(T) = \Gamma_0 + \Gamma_{LA} + \Gamma_{LO} + \Gamma_{imp} = \Gamma_0 + \gamma_{LA}T + \frac{\Gamma_{LO}}{\exp\left(\hbar\bar{\omega}/k_BT\right)-1} + \Gamma_{imp}\exp\left(-E_b/k_BT\right) \quad (1)$$

,where the first term Γ_0 is the temperature-independent inhomogeneous broadening, that is related with the electron-electron interactions, impurities, dislocations and so on.[4] Second term is longitudinal acoustic (LA) phonon scattering induced homogeneous broadening, in which γ_{LA} is the coefficient of its LA phonon-exciton (or electron) coupling strength, reflecting the deformation potential interaction that is linearly dependent on temperature. Third term is the broadening contribution of longitudinal optical (LO) phonon-exciton (or electron) coupling describing the Fröhlich interaction between electrons and the longitudinal electric field generated by LO phonon modes, where Γ_{LO} is the coupling strength of LO phonon-exciton (or electron), $\hbar\bar{\omega}$ is corresponding to phonon energy, relating to the frequency of weakly dispersive LO phonon branch. The last term is the broadening on account of scattering of ionized impurities which is determined by their average binding energy E_b. According to the previous report, since the perovskite is a polar semiconductor, the contribution of Γ_{LA} and Γ_{imp} is insignificant comparing with that of Γ_0 and Γ_{LO}, so these two terms can be neglected here[5,6]. Furthermore, the variation of phonon energy as a function of temperature is also ignored. Hence, the correlation between the FWHM of chiral and achiral 2D perovskite and temperature was fitted via the LO phonon dominating model. It can be simplified as following Equation 2[4]:

$$\Gamma(T) = \Gamma_0 + \frac{\Gamma_{LO}}{exp\left(\frac{E_{LO}}{k_BT}\right)-1} \quad (2)$$

where Γ_0 is a temperature-independent constant that arises from scattering due to structural disorder/imperfection scattering,[7,8] Γ_{LO} is the exciton–longitudinal optical (LO) phonon coupling strength, E_{LO} is the longitudinal optical phonon energy, T is the temperature, and k_B is the Boltzmann constant. The FWHM of the absorption and PL spectrum is extracted, and then fitted the curve according to Equation 2 as shown in (Fig. 4e-h).

Within the harmonic approximation, the phonon dispersion spectra of Rac/S-Br-MBABr (n=1) were calculated using the PHONONPY code (Figure 5a-b). These phonon spectra lack consideration of thermal vibrations or entropy effects. Additionally, the complex interactions between organic molecules and the Pb-Br layer give rise to certain soft modes, resulting in the emergence of imaginary frequencies. This phenomenon is commonly observed in organic-inorganic hybrid perovskites[9,10].The imaginary phonon modes with a negative frequency is possible to be eliminated through distortions of the crystal lattice[11,12].

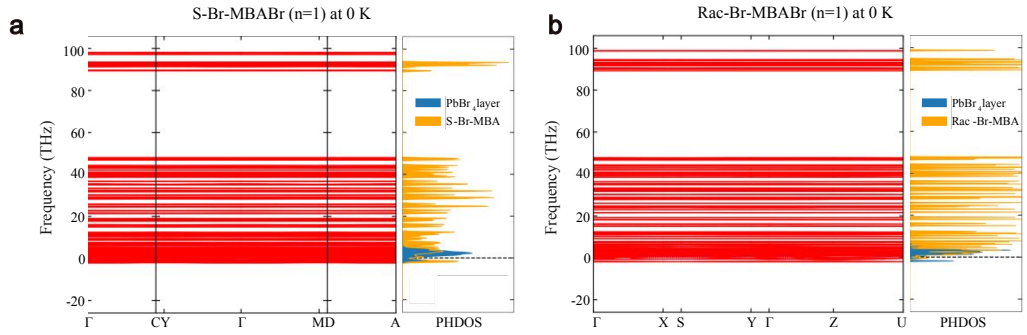

Figure. S15 Phonon band structure and phonon density of states (PHDOS) of S-Br-MBABr (n=1) and Rac-Br-MBABr (n=1) at 0 K.

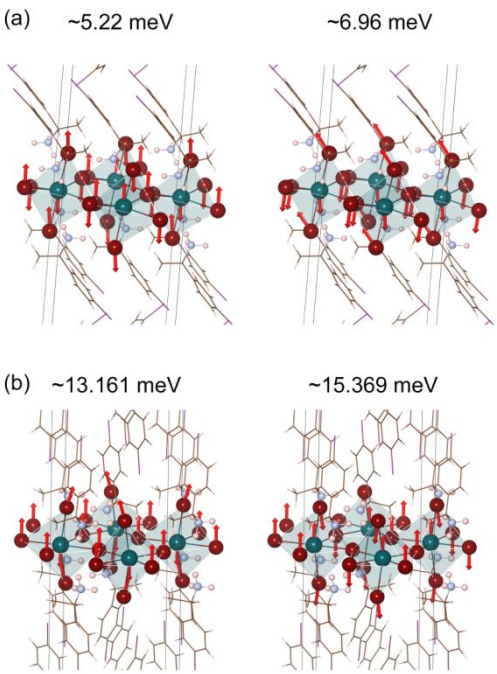

Figure. S16 Participating LO phonon modes in (a) S-Br-MBABr (n=1) and (b) Rac-Br-MBABr (n=1), respectively.

Supplementary Note 2. The calculation of distortion degree of the intra-octahedron

To quantify the average distortion degree of the intra-octahedron, the distortion index (D, bond length), bond angle variance (σ^2), bond length quadratic elongation ($\langle\lambda\rangle$) and effective coordination number (CN_{eff}) is introduced.

1. Distortion Index (D) – Bond Length Distortion

The distortion index D measures the deviation of individual bond lengths from the average bond length within an octahedron. It is defined as:

$$D = \frac{1}{6}\sum_{\{i=1\}}^{6}\frac{|d_i - d_0|}{d_0}$$

d_i denotes the six Pb–X bond lengths, d_0 is the mean M–X bond length. D is dimensionless; a value of 0 indicates a perfectly regular octahedron.

2. Bond Angle Variance (σ^2)

The bond angle variance quantifies the deviation of the ligand–metal–ligand angles from the ideal octahedral value (90° for adjacent ligands, 180° for trans ligands). It is calculated as:

$$\sigma^2 = \left(\frac{1}{11}\right)\sum_{\{i=1\}}^{12}(\theta_i - 90)^2$$

θ_i corresponds to the octahedra Br−Pb−Br bond angles. σ^2 is in deg²; a larger value indicates greater angular distortion.

3. Bond Length Quadratic Elongation ($\langle\lambda\rangle$)

The quadratic elongation provides a normalized measure of bond length distortion relative to an ideal polyhedron. For an octahedron, it is defined as:

$$\langle\lambda\rangle = \frac{1}{6}\sum_{\{i=1\}}^{6}\left(\frac{d_i}{d_o}\right)^2$$

d_i denotes the six Pb–X bond lengths, d_0 is the mean M–X bond length. $\langle\lambda\rangle$ is dimensionless; a value of 1 indicates no distortion, while values >1 indicate bond-length dispersion.

4. Effective Coordination Number (CN_{eff})

The effective coordination number (CN_{eff}) for each metal site was calculated based on the bond-valence approach using the formula:

$$CN_{eff} = \sum_i \exp\left[\frac{d_0 - d_i}{B}\right]$$

where d_i represents the individual bond length, d_0 is the mean M–X bond length, and B is an empirical constant. The summation runs over all bonds within a defined cutoff distance. This method accounts for bond-length distortions and provides a continuous measure of coordination, which is particularly useful for comparing slightly distorted polyhedral environments. All computational procedures are described in full detail, and the software tools used (e.g., VESTA) are cited appropriately.

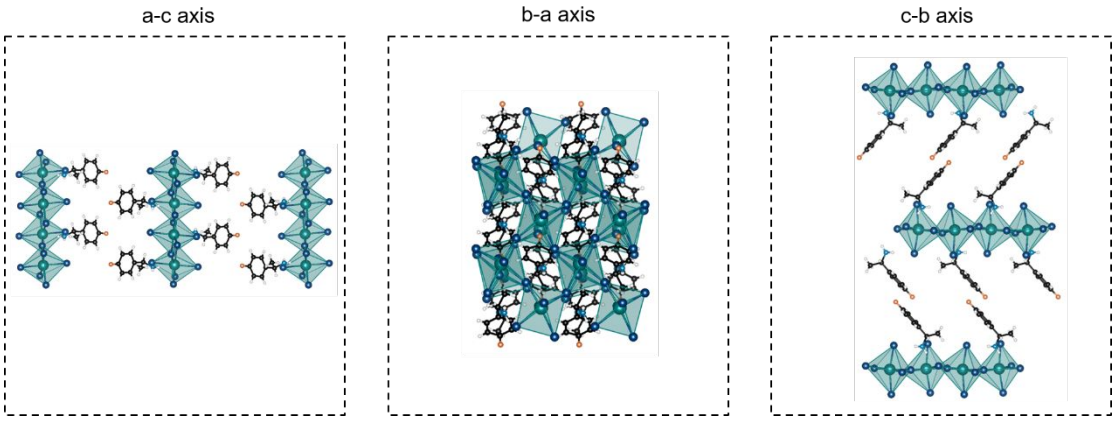

Figure. S17 Crystal structure of S-F-MBABr (n=1) with indicated view axis.

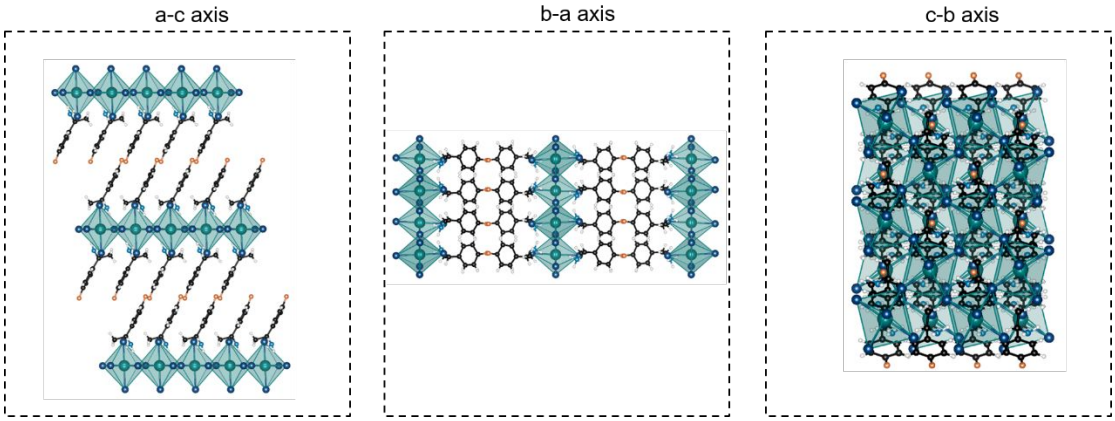

Figure. S18 Crystal structure of Rac-F-MBABr (n=1) with indicated view axis.

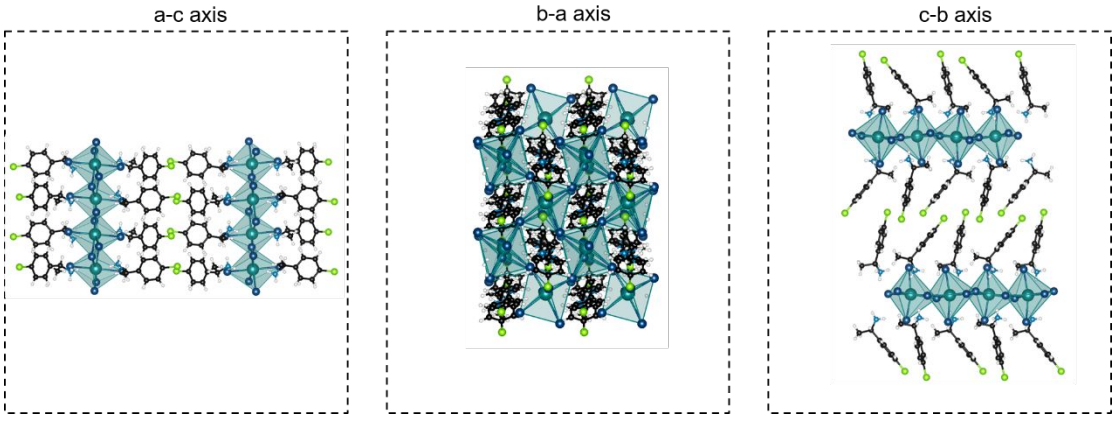

Figure. S19 Crystal structure of S-Cl-MBABr (n=1) with indicated view axis.

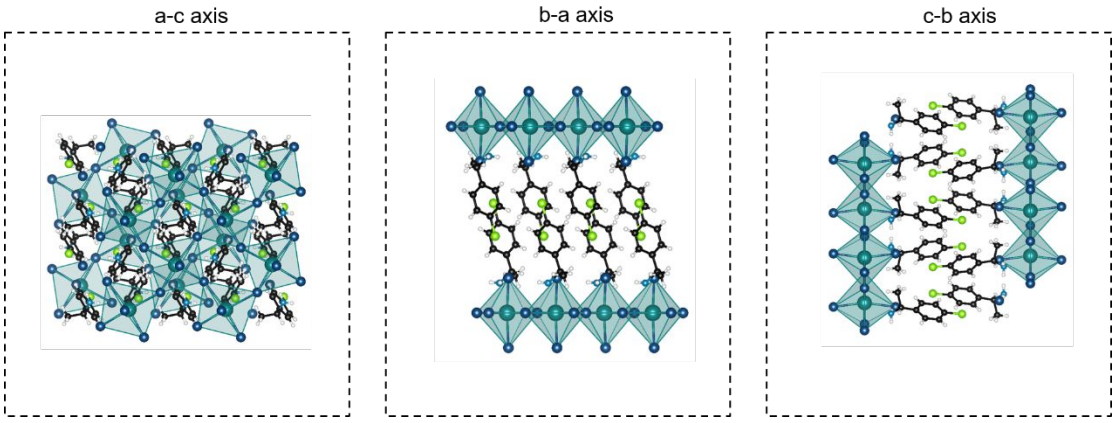

Figure. S20 Crystal structure of Rac-Cl-MBABr (n=1) with indicated view axis.

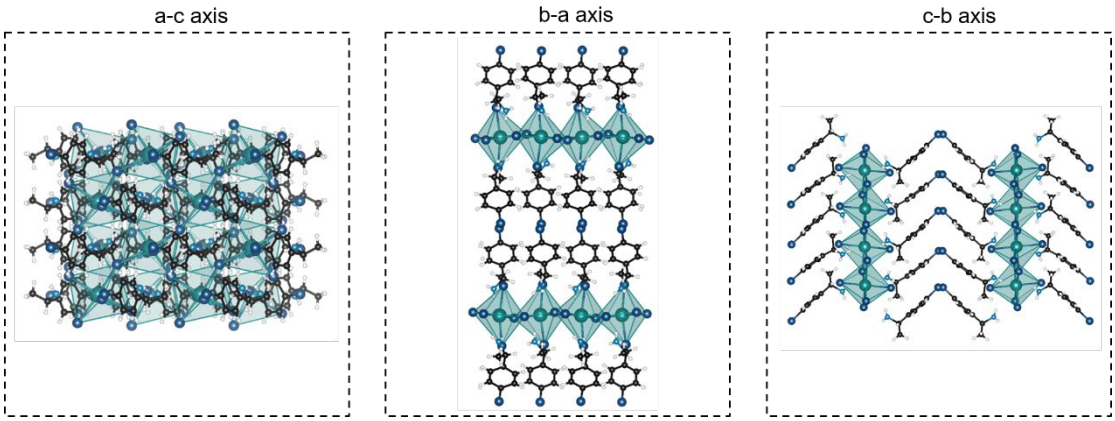

Figure. S21 Crystal structure of S-Br-MBABr (n=1) with indicated view axis.

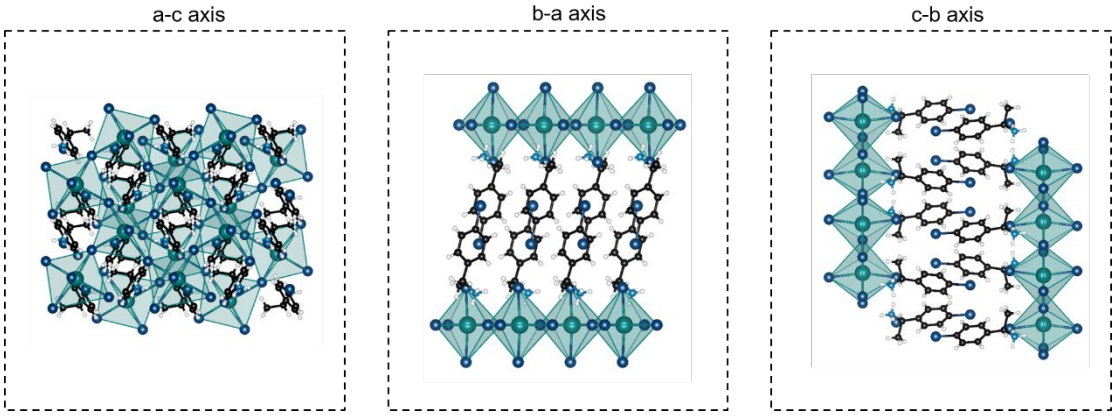

Figure. S22 Crystal structure of Rac-Br-MBABr (n=1) with indicated view axis.

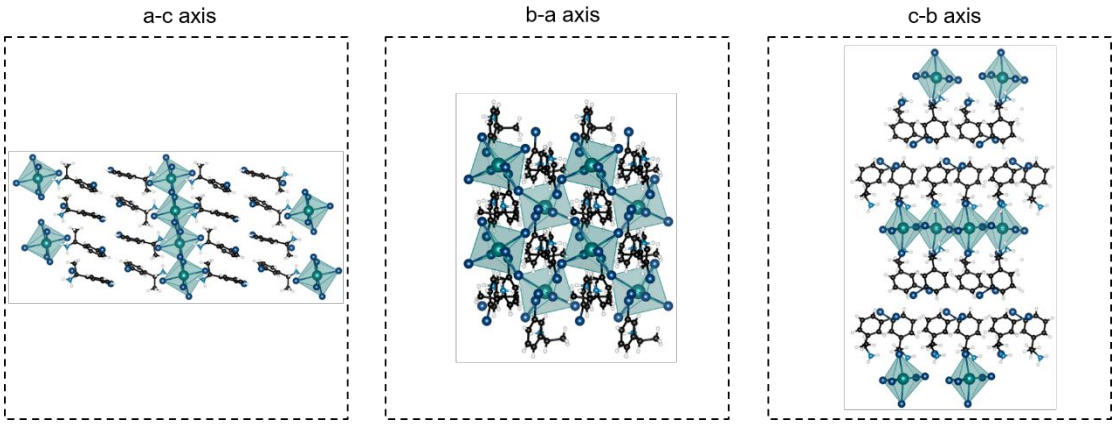

Figure. S23 Crystal structure of S-3Br-MBABr (n=1) with indicated view axis.

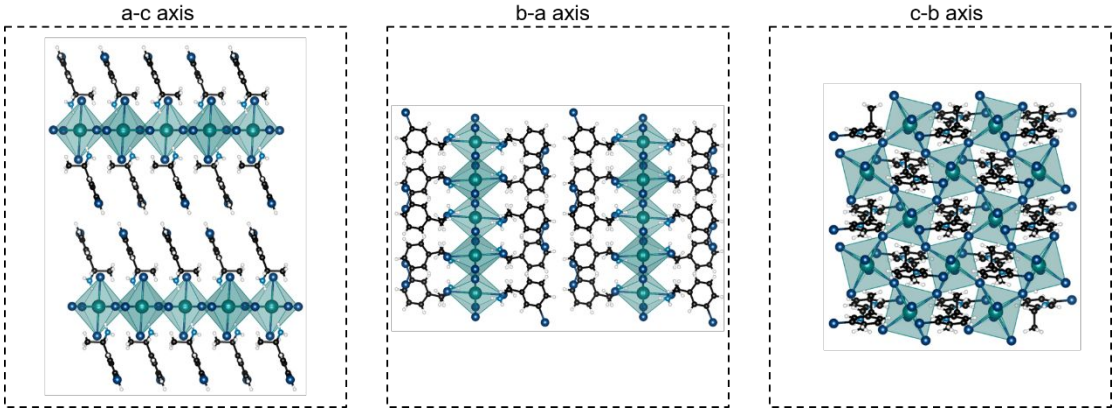

Figure. S24 Crystal structure of Rac-3Br-MBABr (n=1) with indicated view axis.

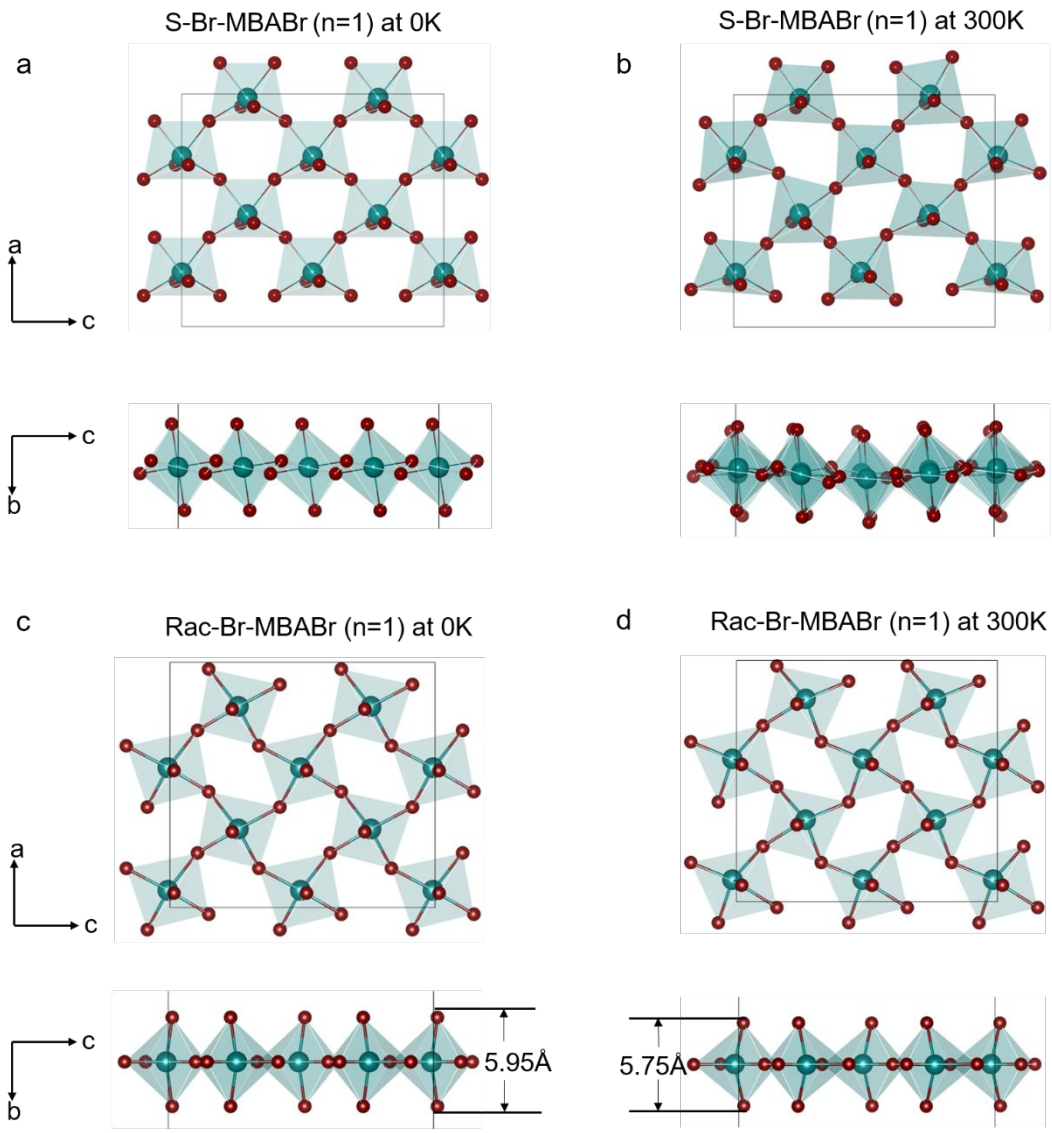

Figure. S25 Top view and side view of crystal structure of S-Br-MBABr (n=1) and Rac-Br-MBABr (n=1) at 0 and 300 K, respectively.

By averaging the atomic positions from the last 10*p*s (5000 steps with a 2*f*s step) of AIMD simulations, it was determined that the root cause stems from the different interactions of organic molecules with the Pb-Br layers. In S-Br-MBABr (n=1), the octahedra effectively mitigates thermal vibrations through twist and rocking motions (Figure. S25a-b), with the bond length deviation increasing only from 0.051 Å at 0 K to 0.0654 Å at 300 K (Table S14). Conversely, the Pb-Br layers in Rac-Br-MBABr (n=1) experience perpendicular compressive stress from organic molecules, resulting in a reduction of the Br-Br distances from 5.95 Å at 0 K to 5.75 Å at 300 K (Figure. S25c-d). This leads to a significant increase in bond length deviation from 0.09 Å at 0 K to 0.23 Å at 300 K (Table S14). Furthermore, the calculated octahedral Distortion Index indicates that Rac-Br-MBABr (n=1) (0.049) exhibits a higher degree of disordering compared to S-Br-MBABr (n=1) (0.019). The smaller distortion index of S-Br-MBABr (n=1) facilitates the energy/excited-state transfer processes.

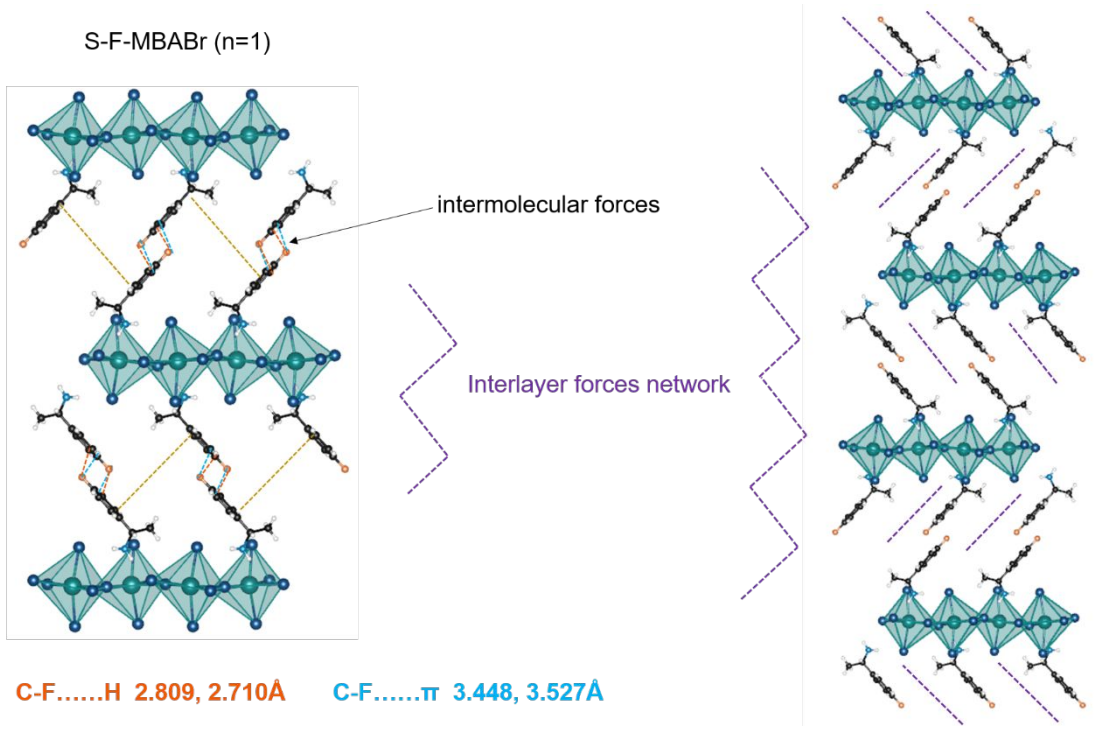

Figure. S26 S-F-MBABr (n=1) perovskite single crystal structure and analysis of intermolecular interaction.

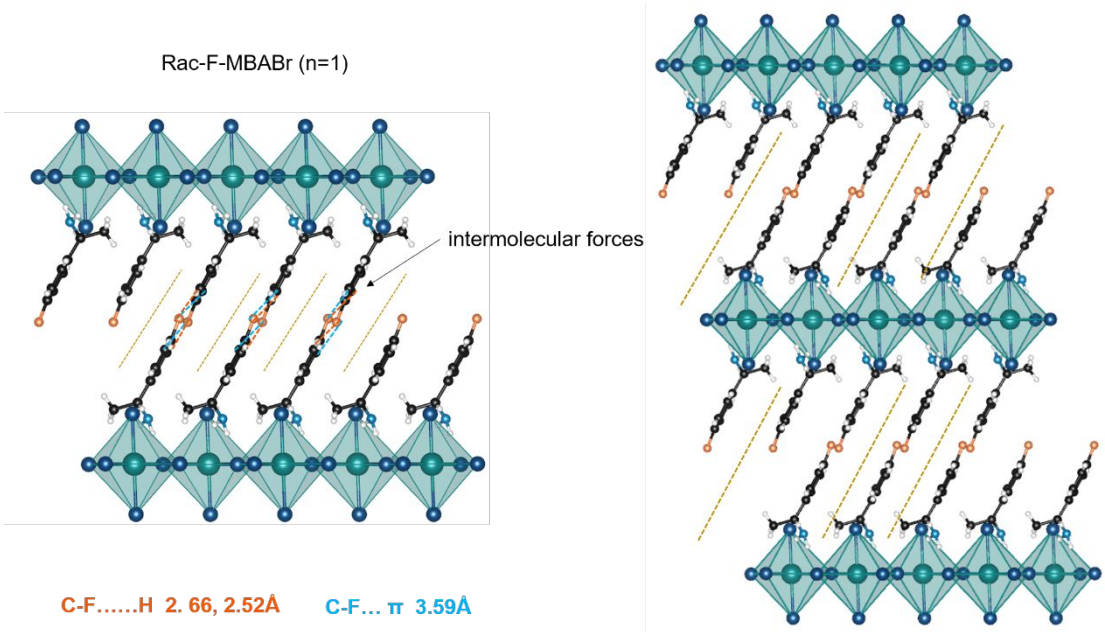

Figure. S27 Rac-F-MBABr (n=1) perovskite single crystal structure and analysis of intermolecular interaction.

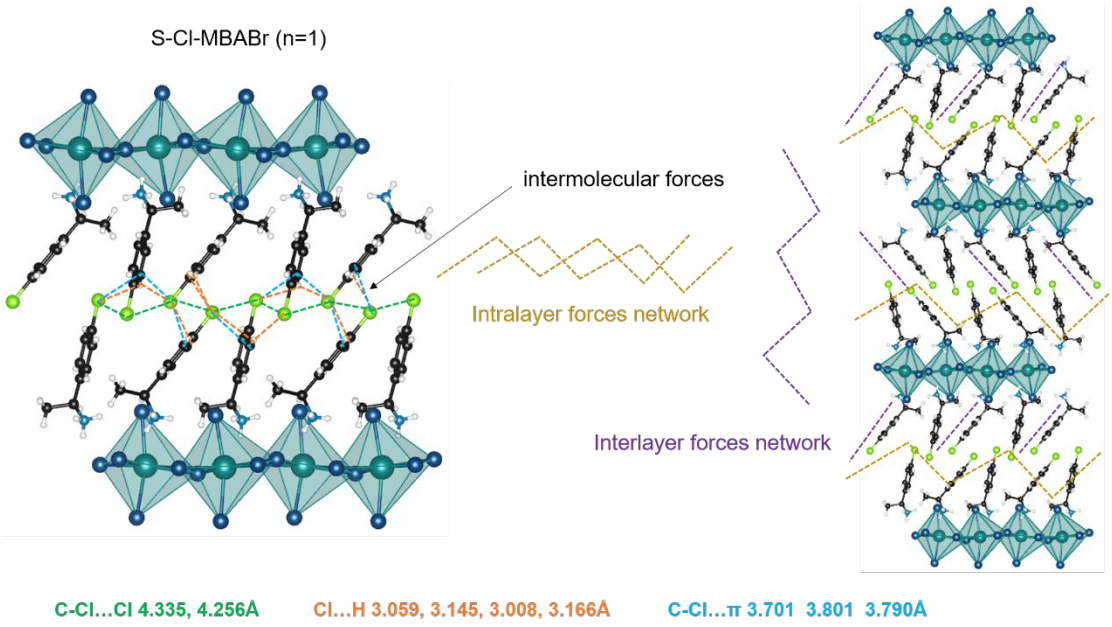

Figure. S28 S-Cl-MBABr (n=1) perovskite single crystal structure and analysis of intermolecular interaction.

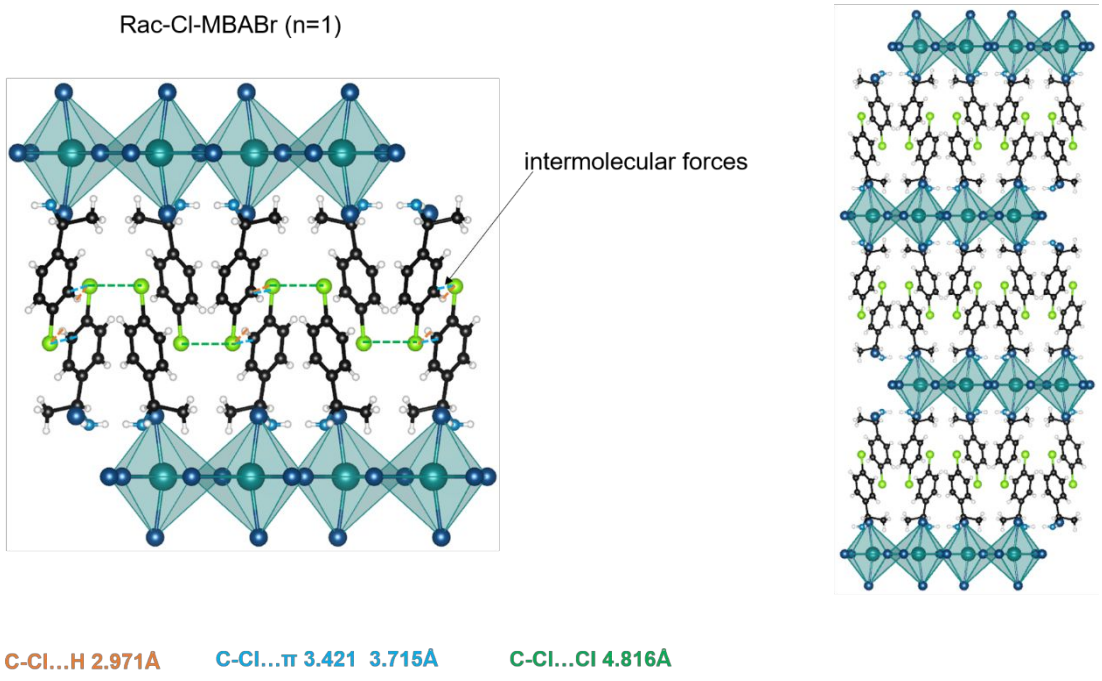

Figure. S29 Rac-Cl-MBABr (n=1) perovskite single crystal structure and analysis of intermolecular interaction.

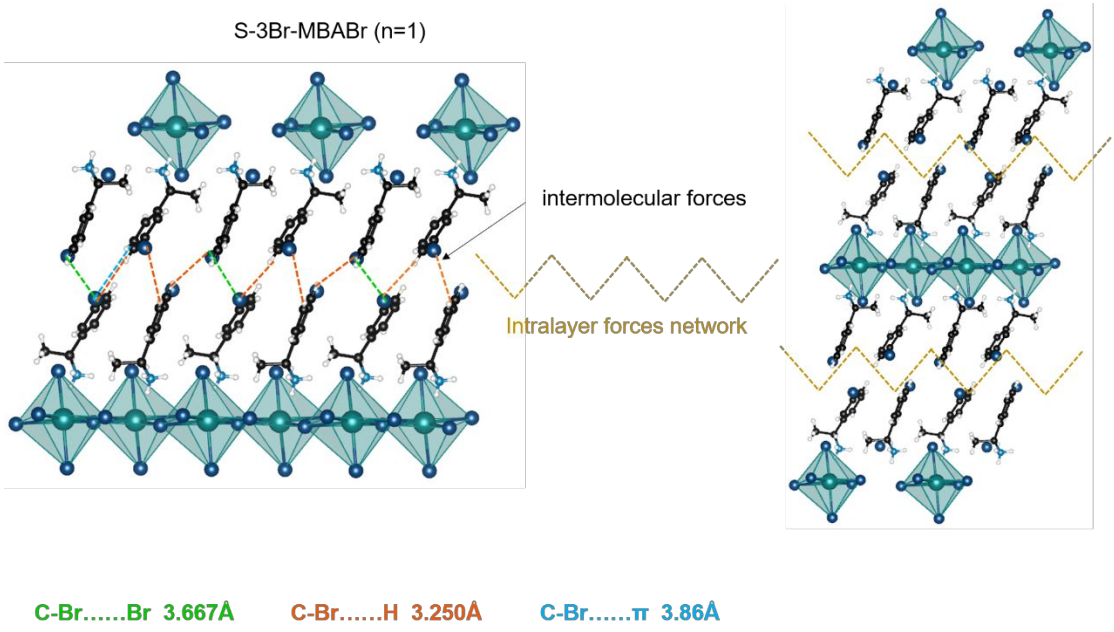

Figure. S30 S-3Br-MBABr (n=1) perovskite single crystal structure and analysis of intermolecular interaction.

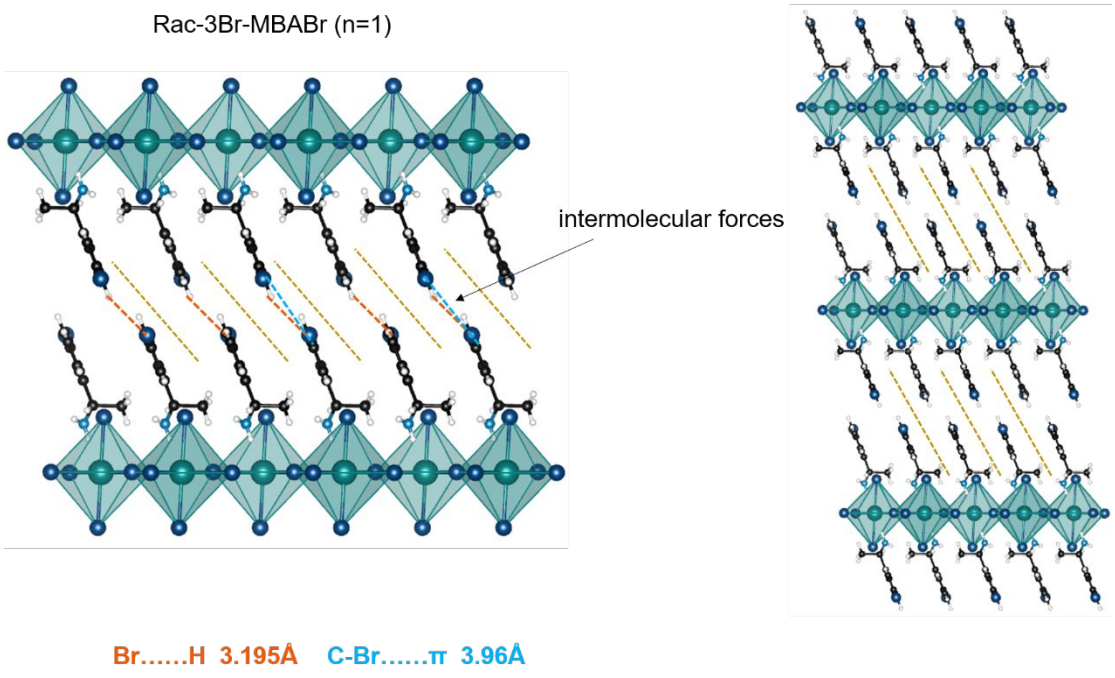

Figure. S31 Rac-3Br-MBABr (n=1) perovskite single crystal structure and analysis of intermolecular interaction.

The organic molecules in S-Br-MBABr (n = 1) are centrosymmetric concerning the Pb-Br octahedra body center (Figure S21). The NH_3 groups of the organic molecules engage with the centrosymmetric facets of the Pb-Br octahedra, inducing twist motions within the octahedra. However, in Rac-Br-MBABr (n = 1), the organic molecules display mirror symmetry relative to the Pb-Br octahedral layers (Figure S22). These molecules interact

nearly perpendicularly with the interstitial spaces between Pb-Br octahedral layers, applying axial compressive forces on the octahedra. The extent of axial compression within Pb-Br octahedral layers varies due to size and electronegativity differences between NH_3 and CH_3 groups.

S-F–MBA (n=1) crystallizes in orthorhombic perovskite with the organic modules aligned parallel to one other (Figure S17). The hydrogen of the phenyl ring, having a partial positive charge (the nucleophile), is attracted electrostatically to the negative potential belt surrounding the C-F bond in the neighbouring molecule (electrophilic site), mainly producing a network of hydrogen bonding (H···B) between A sites. The S-F-MBA molecules adopt an antiparallel arrangement between layers, thereby forming a zigzag-shaped, mechanically interlocked network of intermolecular interactions (Figure S26). S-X-MBA molecules (X=Cl, Br) crystallize in an orthorhombic structure, with an antiparallel fashion in interlayer or intralayer. The electron-poor *σ*-hole site at the halogen forms a short contact with the *π*-electron density of two carbons from the adjacent benzene ring S-3Br-MBA can form an analogous network structure through the combined effects of XB and H···B, as described above (Figure S30).

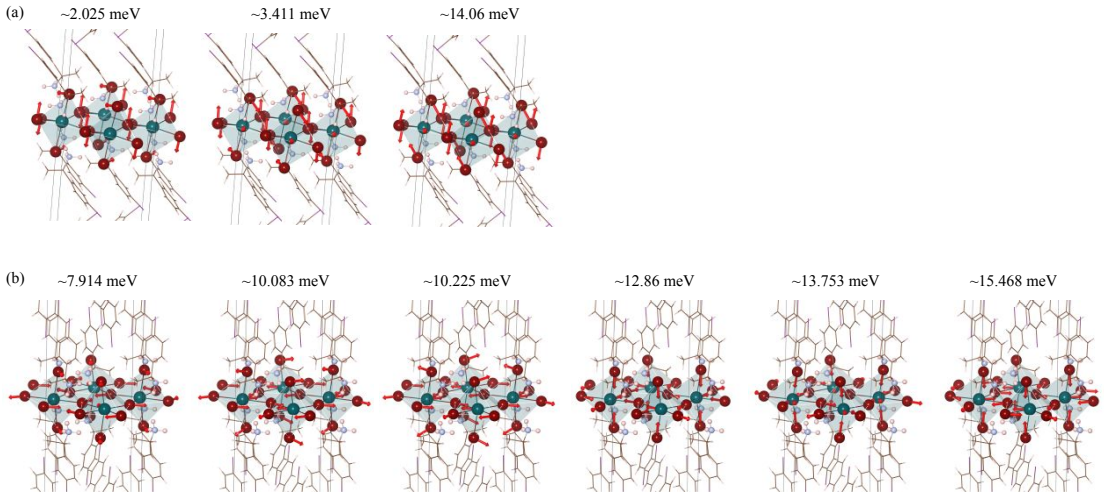

Figure. S32 Participating phonon vibration modes associated with (a) octahedral twisting in S-Br-MBABr (n=1) and (b) octahedral compression in Rac-Br-MBABr (n=1), respectively.

The electronic band structure analysis reveals that the valence band maximum (VBM) of Rac/S-Br-MBABr (n=1) predominantly arises from the antibonding contributions of Pb-6*s* and Br-4*p* orbitals, while the conduction band minimum (CBM) is primarily derived from Pb-6*p* orbitals (Figure. S33), consistent with previous studies[13,14].

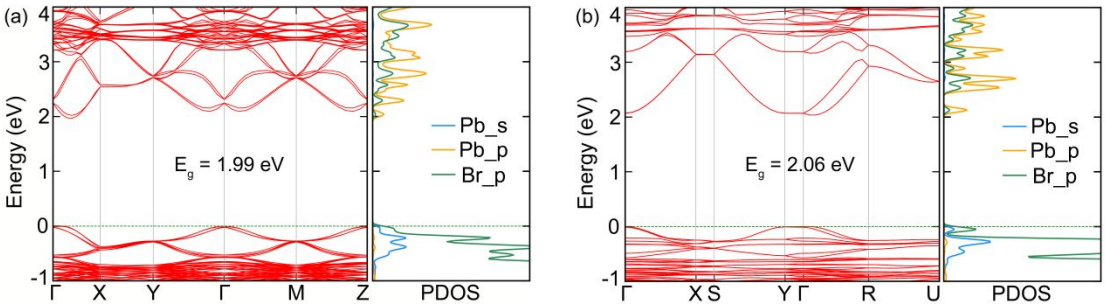

Figure. S33 The electronic band structure and orbital projected partial density of states (PDOS) of (a) S-Br-MBABr (n=1) and (b) Rac-Br-MBABr (n=1), respectively.

Lasing properties

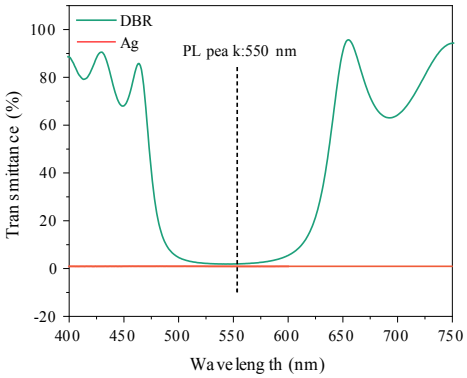

Figure. S34 Transmission spectra of the DBR mirror and Ag mirror. The lasing wavelength is shown with a dashed line.

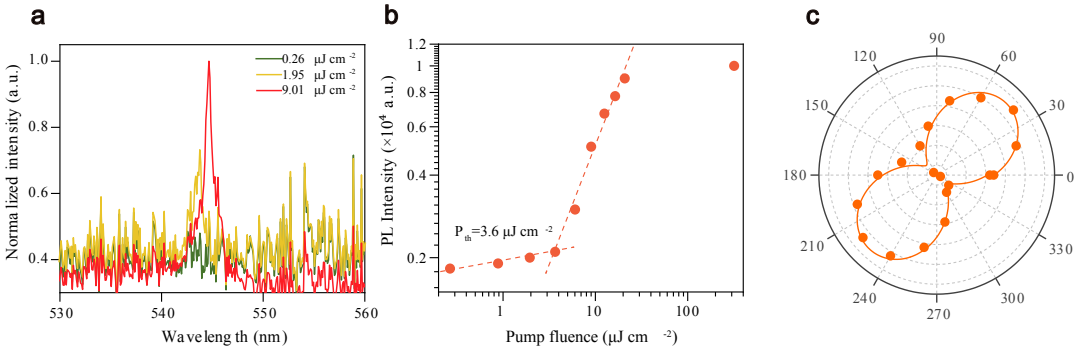

Figure. S35 (a) Rise of the pulse pumped lasing peak centered at ~555 nm with a narrow central mode visible. (b) The integrated intensity of the 555 nm peak has an S-shaped power dependence, with a superlinear transition phase around a threshold of 3.6 μJ/cm^2 giving way to a linear response when the lasing threshold is surpassed. (c) Polar plots of emission intensity at pump fluences above the threshold.

Figure. S36 The green output beam below threshold value.

Table S1 The ASE threshold of quasi-2D perovskite film.

Year	Perovskite ions	Threshold ($\mu J\ cm^{-2}$)	Threshold lasing	Stability ASE/Lasing
2018[15]	OA−MA−Br	17.8	/	/
2018[16]	NMA−FA−Br NMA−FA−Br/I	8.5 19	/	Continuous pulsed laser excitation for ≈32 h at ambient condition
2018[17]	BA−MA−Br	13.6	12.2 $\mu J\ cm^{-2}$	/
2018[18]	BA−FA−Br	21.5	27.2 $\mu J\ cm^{-2}$	Output lasing continues uninterrupted for longer than 6h
2018[19]	PEA−MA−I	14	/	/
2019[20]	NMA−MA−I	19	36 $\mu J\ cm^{-2}$	/
2020[21]	PEA−FA−Br(n=4)	4.16	10 $\mu J\ cm^{-2}$	/
2020[22]	PEA−Cs−Br (n=5)	2.6	/	/
2020[23]	NMA−FA−I	26	/	/
2020[24]	PEA−FA−Br NMA−FA−Br	33.1 16.7	59 W cm^{-2} 45 W cm^{-2}	0.5 h without degradation (2 kW/cm^2)
2020[25]	BA−Cs−Cl	9.6	6.5 $\mu J\ cm^{-2}$	/
2022[26]	DPEA−Cs−Cl/Br (n=3)	6.5	9.2 $\mu J\ cm^{-2}$	/
2023[27]	BDA-Cs-Br 4AMP-Cs-Br	9.28 12	5.5 $\mu J\ cm^{-2}$ 8.9$\mu J\ cm^{-2}$	55 h (T90, 1.1Pth) 61 h (T90, 1.1Pth)
2024[28]	OA-Rb/Cs-Br	13.5	17.8 $\mu J\ cm^{-2}$	/
This work	**S-BrMBA-FABr (n=2)**	**6.36 $\mu J\ cm^{-2}$**	**1.57** W cm^{-2}	0.5 h without degradation (50% RH 1.6 W/cm^2)

Table.. S2 Best-fitting parameters of the S/Rac-F-MBABr (n=1), S/Rac-Cl-MBABr (n=1), S/Rac-Br-MBABr (n=1), and S/Rac-3Br-MBABr (n=1) perovskites.

Sample	Γ_0 (meV)	Γ_{LO} (meV)	E_{LO} (meV)
S-F-MBABr (n=1)	30.4±0.22	22.5±0.79	30.7±1
Rac-F-MBABr (n=1)	34.8±0.16	30.6±2.69	49.3±2.2
S-Cl-MBABr (n=1)	45.8±0.47	8.64±0.63	22.5±2.5
Rac-Cl-MBABr (n=1)	44.8±0.36	28.2±0.98	28.2±1
S-Br-MBABr (n=1)	57.5±0.03	5.72±2.78	73.5±0.01
Rac-Br-MBABr (n=1)	70.2±0.34	39.6±1.6	65.6±1
S-3Br-MBABr (n=1)	27.7±0.39	25.1±2	34.4±2.2

Rac-3Br-MBABr (n=1)	25.2±0.13	42.1±2.6	51.2±1.5

Table. S3 Crystal data and structure refinement for S-Br-MBABr (n=1).

Identification code	**S-Br-MBABr (n=1)**
Empirical formula	$C_{16}H_{20}Br_6N_2Pb$
Formula weight	926.99
Temperature/K	300.0
Crystal system	orthorhombic
Space group	$P2_12_12$
a/Å	34.826(3)
b/Å	8.0150(5)
c/Å	8.7914(6)
α/°	90
β/°	90
γ/°	90
Volume/Å^3	2454.0(3)
Z	4
ρ_{calc}g/cm^3	2.509
μ/mm^{-1}	16.648
F(000)	1688.0
Crystal size/mm^3	0.15 × 0.08 × 0.02
Radiation	MoKα (λ = 0.71073)
2Θ range for data collection/°	4.634 to 55.014
Index ranges	-45 ≤ h ≤ 45, -9 ≤ k ≤ 10, -11 ≤ l ≤ 11
Reflections collected	16689
Independent reflections	5568 [R_{int} = 0.0673, R_{sigma} = 0.0987]
Data/restraints/parameters	5568/108/216
Goodness-of-fit on F^2	1.066
Final R indexes [I>=2σ (I)]	R_1 = 0.0792, wR_2 = 0.1723
Final R indexes [all data]	R_1 = 0.1338, wR_2 = 0.1918
Largest diff. peak/hole / e Å^{-3}	1.75/-1.92
Flack parameter	0.136(17)

Table. S4 Crystal data and structure refinement for Rac-Br-MBABr (n=1).	
Identification code	**Rac-Br-MBABr (n=1)**
Empirical formula	$C_{16}H_{20}Br_6N_2Pb$
Formula weight	929.00
Temperature/K	298.0
Crystal system	orthorhombic
Space group	Pnma
a/Å	8.3041(6)
b/Å	31.6934(19)
c/Å	8.9826(6)
α/°	90
β/°	90
γ/°	90
Volume/Å^3	2364.1(3)
Z	4
ρ_{calc}g/cm^3	2.610
μ/mm^{-1}	17.281
F(000)	1696.0
Crystal size/mm^3	0.1 × 0.02 × 0.02
Radiation	MoKα (λ = 0.71073)
2Θ range for data collection/°	4.714 to 55.002
Index ranges	-10 ≤ h ≤ 9, -41 ≤ k ≤ 41, -11 ≤ l ≤ 10
Reflections collected	22308
Independent reflections	2763 [R_{int} = 0.1378, R_{sigma} = 0.0832]
Data/restraints/parameters	2763/30/120
Goodness-of-fit on F^2	1.020
Final R indexes [I>=2σ (I)]	R_1 = 0.0479, wR_2 = 0.0872
Final R indexes [all data]	R_1 = 0.1066, wR_2 = 0.1093
Largest diff. peak/hole / e Å^{-3}	1.11/-1.42

Table S5. Crystal data and structure refinement for S-F-MBABr (n=1).	
Identification code	**S-F-MBABr (n=1)**
Empirical formula	$C_{16}H_{20}Br_4F_2N_2Pb$
Formula weight	666.00
Temperature/K	240.0
Crystal system	orthorhombic
Space group	$P2_12_12_1$
a/Å	7.8545(3)
b/Å	8.8030(4)
c/Å	33.5312(16)
α/°	90
β/°	90
γ/°	90
Volume/Å^3	2318.45(18)
Z	4
ρ_{calc}g/cm^3	1.908
μ/mm^{-1}	14.159
F(000)	1184.0
Crystal size/mm^3	0.22 × 0.18 × 0.02
Radiation	MoKα (λ = 0.71073)
2Θ range for data collection/°	4.784 to 54.958
Index ranges	-10 ≤ h ≤ 9, -11 ≤ k ≤ 11, -43 ≤ l ≤ 43
Reflections collected	43922
Independent reflections	5276 [R_{int} = 0.0886, R_{sigma} = 0.0555]
Data/restraints/parameters	5276/36/126
Goodness-of-fit on F^2	1.040
Final R indexes [I>=2σ (I)]	R_1 = 0.0456, wR_2 = 0.1314
Final R indexes [all data]	R_1 = 0.0555, wR_2 = 0.1370
Largest diff. peak/hole / e Å^{-3}	1.85/-2.15
Flack parameter	0.024(8)

Table. S6 Crystal data and structure refinement for Rac-F-MBABr (n=1).

Identification code	**Rac-F-MBABr (n=1)**
Empirical formula	$C_{16}H_{20}Br_4F_2N_2Pb$
Formula weight	809.31
Temperature/K	220.0
Crystal system	monoclinic
Space group	C2/c
a/Å	34.513(5)
b/Å	7.9690(9)
c/Å	8.7920(11)
α/°	90
β/°	99.917(8)
γ/°	90
Volume/Å^3	2382.0(5)
Z	4
ρ_{calc}g/cm^3	2.257
μ/mm^{-1}	13.951
F(000)	1487.0
Crystal size/mm^3	0.15 × 0.08 × 0.02
Radiation	MoKα (λ = 0.71073)
2Θ range for data collection/°	5.25 to 54.968
Index ranges	-44 ≤ h ≤ 44, -9 ≤ k ≤ 10, -11 ≤ l ≤ 11
Reflections collected	32267
Independent reflections	2682 [R_{int} = 0.0795, R_{sigma} = 0.0471]
Data/restraints/parameters	2682/78/144
Goodness-of-fit on F^2	1.013
Final R indexes [I>=2σ (I)]	R_1 = 0.1008, wR_2 = 0.2159
Final R indexes [all data]	R_1 = 0.1050, wR_2 = 0.2177
Largest diff. peak/hole / e Å^{-3}	1.53/-1.57

Table. S7 Crystal data and structure refinement for S-Cl-MBABr (n=1).

Identification code	**S-Cl-MBABr (n=1)**
Empirical formula	$C_{16}H_{22}Br_4Cl_2N_2Pb$
Formula weight	840.08
Temperature/K	299.4(3)
Crystal system	orthorhombic
Space group	$P2_12_12_1$
a/Å	7.9135(3)
b/Å	8.8066(3)
c/Å	35.5777(18)
α/°	90
β/°	90
γ/°	90
Volume/Å^3	2479.45(18)
Z	4
ρ_{calc}g/cm^3	2.250
μ/mm^{-1}	13.470
F(000)	1552.0
Crystal size/mm^3	0.34 × 0.28 × 0.15
Radiation	Mo Kα (λ = 0.71073)
2Θ range for data collection/°	4.58 to 61.592
Index ranges	-10 ≤ h ≤ 8, -11 ≤ k ≤ 12, -36 ≤ l ≤ 46
Reflections collected	13380
Independent reflections	5846 [R_{int} = 0.0303, R_{sigma} = 0.0428]
Data/restraints/parameters	5846/0/230
Goodness-of-fit on F^2	1.033
Final R indexes [I>=2σ (I)]	R_1 = 0.0368, wR_2 = 0.0797
Final R indexes [all data]	R_1 = 0.0544, wR_2 = 0.0848
Largest diff. peak/hole / e Å^{-3}	1.61/-1.43
Flack parameter	-0.024(8)

Table. S8 Crystal data and structure refinement for Rac-Cl-MBABr (n=1).

Identification code	**Rac-Cl-MBABr (n=1)**
Empirical formula	$C_{16}H_{20}Br_4Cl_2N_2Pb$
Formula weight	838.07
Temperature/K	220.0
Crystal system	orthorhombic
Space group	Pnma
a/Å	8.2230(3)
b/Å	31.4618(14)
c/Å	8.8943(4)
α/°	90
β/°	90
γ/°	90
Volume/Å^3	2301.05(17)
Z	4
ρ_{calc}g/cm^3	2.419
μ/mm^{-1}	14.514
F(000)	1544.0
Crystal size/mm^3	0.18 × 0.04 × 0.04
Radiation	MoKα (λ = 0.71073)
2Θ range for data collection/°	4.76 to 55.066
Index ranges	-10 ≤ h ≤ 9, -40 ≤ k ≤ 40, -11 ≤ l ≤ 11
Reflections collected	70894
Independent reflections	2684 [R_{int} = 0.0851, R_{sigma} = 0.0293]
Data/restraints/parameters	2684/0/125
Goodness-of-fit on F^2	1.004
Final R indexes [I>=2σ (I)]	R_1 = 0.0395, wR_2 = 0.0833
Final R indexes [all data]	R_1 = 0.0449, wR_2 = 0.0856
Largest diff. peak/hole / e Å^{-3}	1.51/-2.25

Table. S9 Crystal data and structure refinement for S-3Br-MBABr (n=1).

Identification code	**S-3Br-MBABr (n=1)**
Empirical formula	$C_{16}H_{22}Br_6N_2Pb$
Formula weight	929.00
Temperature/K	299.70(10)
Crystal system	monoclinic
Space group	$P2_1$
a/Å	8.7920(2)
b/Å	7.88540(10)
c/Å	18.0045(3)
α/°	90
β/°	97.500(2)
γ/°	90
Volume/Å^3	1237.55(4)
Z	2
ρ_{calc}g/cm^3	2.493
μ/mm^{-1}	24.629
F(000)	848.0
Crystal size/mm^3	0.04 × 0.04 × 0.01
Radiation	Cu Kα (λ = 1.54184)
2Θ range for data collection/°	10.148 to 129.934
Index ranges	-10 ≤ h ≤ 10, -9 ≤ k ≤ 9, -21 ≤ l ≤ 21
Reflections collected	21337
Independent reflections	4191 [R_{int} = 0.0776, R_{sigma} = 0.0334]
Data/restraints/parameters	4191/1/230
Goodness-of-fit on F^2	1.056
Final R indexes [I>=2σ (I)]	R_1 = 0.0427, wR_2 = 0.1122
Final R indexes [all data]	R_1 = 0.0427, wR_2 = 0.1122
Largest diff. peak/hole / e Å^{-3}	1.25/-2.80
Flack parameter	0.004(9)

Table. S10 Crystal data and structure refinement for Rac-3Br-MBABr (n=1).

Identification code	**Rac-3Br-MBABr (n=1)**
Empirical formula	$C_{16}H_{20}Br_6N_2Pb$
Formula weight	926.99
Temperature/K	306.0
Crystal system	monoclinic
Space group	$P2_1/c$
a/Å	17.920(5)
b/Å	8.000(3)
c/Å	8.761(3)
α/°	90
β/°	96.051(11)
γ/°	90
Volume/Å^3	1249.1(7)
Z	2
ρ_{calc}g/cm^3	2.465
μ/mm^{-1}	16.354
F(000)	844.0
Crystal size/mm^3	0.18 × 0.08 × 0.02
Radiation	MoKα (λ = 0.71073)
2Θ range for data collection/°	5.582 to 55.094
Index ranges	-23 ≤ h ≤ 23, -10 ≤ k ≤ 9, -10 ≤ l ≤ 11
Reflections collected	12253
Independent reflections	2832 [R_{int} = 0.0435, R_{sigma} = 0.0493]
Data/restraints/parameters	2832/60/104
Goodness-of-fit on F^2	1.154
Final R indexes [I>=2σ (I)]	R_1 = 0.1111, wR_2 = 0.2691
Final R indexes [all data]	R_1 = 0.1166, wR_2 = 0.2720
Largest diff. peak/hole / e Å^{-3}	3.47/-1.67

Table. S11 Crystal data and structure refinement for S/Rac-*Br-MBABr (n=1)*.

Structure	**S-Br-MBABr (n=1)**	**Rac-Br-MBABr (n=1)**
Pb-Br bond length	2.929(18) 2.991(4) 2.998(15) 3.050(3) 3.056(3) 3.184(4)	3.3172(18) 3.3117(17) 3.0670(17) 2.8950(17) 2.9726(10) 2.9726(10)
Average Pb-Br bond length (Å)	3.0346	3.0893
Standard deviation of bond length	0.0864	0.1826
Difference between maximum and minimum bond lengths (Å)	0.255	0.4222
Average quadratic elongation λ	1.0003	1.0029
Average equatorial Pb−Br−Pb angles(β)	152°	153°
Difference between maximum and minimum bond angle (deg/ in plane) Δβ	11.4	10.8
Distortion index (bond length)	0.0204	0.0485
Effective coordination number	5.842	5.280
Bond angle variance	39	36
Optical bandgap (eV)	3.74	3.91

Table. S12 The bonding analysis (bond length and integrated crystal orbital Hamilton population (ICOHP)) for the nearest neighbor and next nearest neighbor N-H···Br bond in $(S\text{-}Br\text{-}MBA)_2PbBr_4$ and $(Rac\text{-}Br\text{-}MBA)_2PbBr_4$ perovskites

Name	**Nearest neighbor N-H···Br bond length(Å)**	**Next nearest neighbor N-H···Br bond (Å)**
S-Br-MBABr (n=1)	2.405	2.477
Rac-Br-MBABr (n=1)	2.303	2.391

Table S13 Bader charge analysis of different groups in $(S\text{-}Br\text{-}MBA)_2PbBr_4$ and $(Rac\text{-}Br\text{-}MBA)_2PbBr_4$ perovskites.

Name	**$PbBr_4$**	**NH_3**	**CH**	**CH_3**
S-Br-MBABr (n=1)	1.518	-0.333	-0.336	-0.061
Rac-Br-MBABr (n=1)	1.473	-0.313	-0.330	-0.072

Table. S14 Crystallographic information of S-Br-MBABr (n=1) and Rac-Br-MBABr (n=1) perovskites at 0 and 300 K via DFT calculation, respectively.

Structure	S-Br-MBABr (n=1) at 0 K	Rac-Br-MBABr (n=1) at 0 K	S-Br-MBABr (n=1) at 300 K	Rac-Br-MBABr (n=1) at 300 K
Pb-Br bond length (Å)	2.99722(0) 2.99722(0) 3.02553(0) 3.02553(0) 3.04885(0) 3.04885(0)	2.97361(0) 3.00723(0) 3.00724(0) 3.14990(0) 3.17165(0) 3.19306(0)	2.92773(0) 2.98194(0) 2.98330(0) 2.98531(0) 3.06475(0) 3.12782(0)	2.93565 (0) 2.98706 (0) 3.06518 (0) 3.06830 (0) 3.08402 (0) 3.57570 (0)
Average Pb-Br bond length (Å)	3.0239	3.0838	3.0118	3.0893
Standard deviation of bond length (Å)	0.051	0.090	0.0654	0.23
Difference between maximum and minimum bond lengths (Å)	0.138	0.219	0.20	0.64
Average quadratic elongation **λ**	1.0535	1.0135	1.0222	1.0470
Average equatorial Pb−Br−Pb angles (β, deg.)	153.3; 153.3	158.7;145.5	139.8; 150.8;162.6	132.3;164.4
Difference between maximum and minimum bond angle (deg./ in plane)	0	13.2	22.8	31.7
Distortion index (bond length)	0.00588	0.02846	0.019	0.049

Table. S15 Crystal data and structure refinement for S-*X-MBABr (n=1) and* S-*3X-MBABr (n=1)*. X: F, Cl, Br

2D perovskite	Space Groups	Distortion index D	Bond angle variance σ^2	Bond angle Difference $\Delta\beta$
S-F-MBABr (n=1)	P 21 21 21	0.0304	49.56	14.57
Rac-F-MBABr (n=1)	C 2/c	0.0117	15.76	0
S-Cl-MBABr (n=1)	P 21 21 21	0.0316	49.64	14.87
Rac-Cl-MBABr (n=1)	P n m a	0.0419	36.67	11.7
S-3F-MBABr (n=1)	P 21	0.0211	53.45	14.22
S-3Cl-MBABr (n=1)	P 21	0.0186	48.66	14.18
S-3Br-MBABr (n=1)	P 21	0.0180	45.11	14.12
Rac-3Br-MBABr (n=1)	P 21/c	0.0107	17.98	0

Table. S16 Statistical Analysis of Perovskite Continuous Wave Lasing Threshold

Materials	*type*	*Pump source*	*T(K)*	*λ(nm)*	*Threshold ($W\ cm^{-2}$)*	*δλ(nm)*	*Year*
$MAPbI_3$ thin films	DFB	20ns, 2MHz	160	790	5k	1	2016[29]
$MAPbI_3$ thin films	DFB	445 nm, 920 ns,100 Hz	102	785	17k	0.25	2017[30]
$CsPbBr_3$ NWs	FP	CW (405 nm)	4	524	1.45nw	0.09	2018[31]
$CsPbBr_3$ NWs	FP	CW (450 nm)	77	533	6k	0.23	2018[32]
$MAPbBr_3$ QD films	DFB	CW (405 nm)	RT	538.7	15	0.45	2019[33]
$MAPbCl_3$ QD films	DFB	CW (405 nm)	RT	482	58	0.45	2019[33]
$MAPbI_3$ QD films	DFB	CW (405 nm)	RT	614	24	0.45	2019[33]
$MAPbBr_3$ single crystal thin films	VCSEL	CW (405nm)	RT	565	34m	0.8	2019[34]
$CsPbBr_3$ nanoribbon	FP	CW (405nm)	<100	530	2.6k	0.3	2020[35]
$NMA_2FAPbBr$	DFB	CW (488 nm)	RT	555	45	0.8	2020[36]
$PEA_2FAPbBr$	DFB	CW (488 nm)	RT	553	59	1	2020[36]
$MAPbI_3$ NCs	FP	CW (405nm)	RT	762	132nw	0.91-1.31	2021[37]
$(PEA)_2PbI_4$ thin flake	VCSEL	CW (488 nm)	RT	537.4	5.7	0.42	2021[38]
$MAPbBr_3$ single crystal nanoplates	VCSEL	CW (488 nm)	80	547.1	55.2	0.44	2021[39]
S-Br-MBABr (n=2)	**VCSEL**	**CW (405 nm)**	**RT**	**556**	**1.57**	**0.3**	**This Work**

References

1. Fu, J., Ramesh, S., Melvin Lim, J. W. & Sum, T. C. Carriers, Quasi-particles, and Collective Excitations in Halide Perovskites. *Chem. Rev.* 123, 8154–8231 (2023).
2. Wu, X. *et al.* Trap states in lead iodide perovskites. *J. Am. Chem. Soc.* 137, 2089–2096 (2015).
3. Zhang, T. *et al.* Regulation of the luminescence mechanism of two-dimensional tin halide perovskites. *Nat. Commun.* 13, 60 (2022).
4. Wright, A. D. *et al.* Electron–phonon coupling in hybrid lead halide perovskites. *Nat. Commun.* 7, 11755 (2016).
5. Guo, Z., Wu, X., Zhu, T., Zhu, X. & Huang, L. Electron-Phonon Scattering in Atomically Thin 2D Perovskites. *ACS Nano* 10, 9992–9998 (2016).
6. Li, Y. *et al.* Phase-pure 2D tin halide perovskite thin flakes for stable lasing. *Sci. Adv.* 9, eadh0517 (2023).
7. Rudin, S., Reinecke, T. L. & Segall, B. *Temperature-Dependent Exciton Linewidths in Semiconductors*. *PHYSICAL REVIEW B* vol. 42.
8. Malikova, L. *et al. PHYSICAL REVIEW B 15 JULY 1996-I VOLUME*. vol. 54 (1996).
9. Chen, X. Y., Zhao, B. Q., Liu, Z., Wei, S. H. & Zhang, X. Crystal-liquid duality enhanced dynamical stability of hybrid perovskites. *Physical Chemistry Chemical Physics* 25, 17787–17792 (2023).
10. Yang, J. *et al.* Acoustic-optical phonon up-conversion and hot-phonon bottleneck in lead-halide perovskites. *Nat. Commun.* 8, 14120 (2017).
11. Kawai, H., Giorgi, G., Marini, A. & Yamashita, K. The Mechanism of Slow Hot-Hole Cooling in Lead-Iodide Perovskite: First-Principles Calculation on Carrier Lifetime

from Electron–Phonon Interaction. *Nano Lett.* 15, 3103–3108 (2015).

12. Motta, C. *et al.* Revealing the role of organic cations in hybrid halide perovskite CH3 NH3PbI3. *Nat. Commun.* 6, 7026 (2015).

13. Yin, W.-J., Shi, T. & Yan, Y. Unusual defect physics in CH3NH3PbI3 perovskite solar cell absorber. *Appl. Phys. Lett.* 104, (2014).

14. Kirstein, E. *et al.* The Landé factors of electrons and holes in lead halide perovskites: universal dependence on the band gap. *Nat. Commun.* 13, (2022).

15. Wang, R. *et al.* Preferential Orientation of Crystals Induced by Incorporation of Organic Ligands in Mixed-Dimensional Hybrid Perovskite Films. *Adv. Opt. Mater.* 6, 1701311 (2018).

16. Li, M. *et al.* Amplified Spontaneous Emission Based on 2D Ruddlesden–Popper Perovskites. *Adv. Funct. Mater.* 28, 1707006 (2018).

17. Zhang, H. *et al.* 2D Ruddlesden–Popper Perovskites Microring Laser Array. *Advanced Materials* 30, 1706186 (2018).

18. Zhang, H. *et al.* A Two-Dimensional Ruddlesden–Popper Perovskite Nanowire Laser Array based on Ultrafast Light-Harvesting Quantum Wells. *Angewandte Chemie* 130, 7874–7878 (2018).

19. Leyden, M. R. *et al.* Amplified spontaneous emission in phenylethylammonium methylammonium lead iodide quasi-2D perovskites. *Physical Chemistry Chemical Physics* 20, 15030–15036 (2018).

20. Leyden, M. R. *et al.* Distributed Feedback Lasers and Light-Emitting Diodes Using 1-Naphthylmethylamnonium Low-Dimensional Perovskite. *ACS Photonics* 6, 460–

466 (2019).

21. Lei, L. *et al.* Efficient Energy Funneling in Quasi-2D Perovskites: From Light Emission to Lasing. *Advanced Materials* 32, 1906571 (2020).

22. Cui, M. *et al.* Direct Observation of Competition between Amplified Spontaneous Emission and Auger Recombination in Quasi-Two-Dimensional Perovskites. *Journal of Physical Chemistry Letters* 11, 5734–5740 (2020).

23. Guo, J. *et al.* Ultrashort laser pulse doubling by metal-halide perovskite multiple quantum wells. *Nat. Commun.* 11, 3361 (2020).

24. Qin, C. *et al.* Stable room-temperature continuous-wave lasing in quasi-2D perovskite films. *Nature* 585, 53–57 (2020).

25. Pina, J. M. *et al.* Deep-Blue Perovskite Single-Mode Lasing through Efficient Vapor-Assisted Chlorination. *Advanced Materials* 33, 2006697 (2021).

26. Wang, C. *et al.* Low-Threshold Blue Quasi-2D Perovskite Laser through Domain Distribution Control. *Nano Lett.* 22, 1338–1344 (2022).

27. Wang, X. *et al. Quasi-2D Dion-Jacobson Phase Perovskites as a Promising Material Platform for Stable and High-Performance Lasers*. https://www.science.org (2023) doi:10.1126/sciadv.adj3476.

28. Lu, G. *et al.* Blue Perovskite Lasing Derived from Bound Excitons through Defect Engineering. *ACS Nano* 18, 23457–23467 (2024).

29. Jia, Y. *et al.* Diode-pumped organo-lead halide perovskite lasing in a metal-clad distributed feedback resonator. *Nano Lett.* 16, 4624–4629 (2016).

30. Jia, Y., Kerner, R. A., Grede, A. J., Rand, B. P. & Giebink, N. C. Continuous-wave

lasing in an organic-inorganic lead halide perovskite semiconductor. *Nat. Photonics* 11, 784–788 (2017).

31. Jiang, L. *et al.* Continuous wave pumped single-mode nanolasers in inorganic perovskites with robust stability and high quantum yield. *Nanoscale* 10, 13565–13571 (2018).

32. Evans, T. J. S. *et al.* Continuous-Wave Lasing in Cesium Lead Bromide Perovskite Nanowires. *Adv. Opt. Mater.* 6, 1700982 (2018).

33. Wang, L. *et al.* Ultralow-Threshold and Color-Tunable Continuous-Wave Lasing at Room-Temperature from in Situ Fabricated Perovskite Quantum Dots. *Journal of Physical Chemistry Letters* 10, 3248–3253 (2019).

34. Tian, C. *et al.* Low-Threshold room-Temperature continuous-wave optical lasing of single-crystalline perovskite in a distributed reflector microcavity. *RSC Adv.* 9, 35984–35989 (2019).

35. Shang, Q. *et al.* Role of the Exciton-Polariton in a Continuous-Wave Optically Pumped CsPbBr3Perovskite Laser. *Nano Lett.* 20, 6636–6643 (2020).

36. Qin, C. *et al.* Stable room-temperature continuous-wave lasing in quasi-2D perovskite films. *Nature* 585, 53–57 (2020).

37. Nguyen, D. H. *et al.* Ultralow-Threshold Continuous-Wave Room-Temperature Crystal-Fiber/Nanoperovskite Hybrid Lasers for All-Optical Photonic Integration. *Advanced Materials* 33, 2006819 (2021).

38. Zhang, H. *et al.* Room-temperature continuous-wave vertical-cavity surface-emitting lasers based on 2D layered organic–inorganic hybrid perovskites. *APL*

Mater. 9, 071106 (2021).

39. Zhang, H. *et al.* Continuous-Wave Vertical Cavity Surface-Emitting Lasers based on Single Crystalline Lead Halide Perovskites. *Adv. Opt. Mater.* 9, 2001982 (2021).